



## Microwave remote sensing of the 2011 Plinian eruption of the Grímsvötn Icelandic volcano

Frank S. Marzano <sup>a,b,\*</sup>, Mirko Lamantea <sup>a</sup>, Mario Montopoli <sup>b,c</sup>, Michael Herzog <sup>c</sup>, Hans Graf <sup>c</sup>, Domenico Cimini <sup>d</sup>

<sup>a</sup> Department of Information Engineering (DIET), Sapienza University of Rome, Rome, Italy

<sup>b</sup> Centre of Excellence CETEMPS, University of L'Aquila, L'Aquila, Italy

<sup>c</sup> Department of Geography, University of Cambridge, Cambridge, UK

<sup>d</sup> IMAA, National Research Council (CNR), Tito Scalo (Potenza), Italy

### ARTICLE INFO

#### Article history:

Received 14 February 2012

Received in revised form 10 September 2012

Accepted 6 November 2012

Available online xxx

#### Keywords:

Volcanic eruption clouds

Ash retrieval

Weather radars

Radar meteorology

Microwave radiometry

Inversion methods

### ABSTRACT

The sub-glacial Plinian explosive eruption of the Grímsvötn volcano, which occurred on May 2011, is for the first time analyzed and quantitatively interpreted by using ground-based weather radar data and the Volcanic Ash Radar Retrieval (VARR) physically-based technique. The prevailing southerly winds stretched the erupted plume toward the Arctic pole, thus preventing the ash cloud to move toward continental Europe and threatening the airline traffic (different from the less explosive Eyjafjöll eruption on April and May 2010). The 2011 Grímsvötn eruption has been continuously monitored by the Keflavík C-band weather radar, located at a distance of about 260 km from the volcano vent. The VARR methodology is summarized and applied to available radar time series to estimate the coarse ash particle category, volume, fallout, concentration and the plume maximum height, every 5 min within the volcano vent surroundings (i.e. an area of about  $100 \times 100 \text{ km}^2$  around the volcano). Due to the large distance from the volcano, fine-grained ash cannot be detected and estimated by the Keflavík C-band weather radar. Estimates of the eruption discharge rate, based on the retrieved ash plume top height, are provided together with an evaluation of the total erupted mass and volume. Deposited ash at ground is also retrieved from radar data by empirically reconstructing the vertical profile of radar reflectivity and estimating the near-surface ash fallout. Radar-based ash retrieval results can be compared with available satellite microwave radiometric imagery in order to show the potential contribution and limitations of these microwave remote sensing products to the understanding and modeling of explosive volcanic ash eruptions. Spaceborne microwave brightness temperatures show a correlation with ash columnar content, derived from VARR, depending on the millimeter-wave frequency and on the spatial averaging. Microphysical sensitivity of satellite microwave brightness temperatures to plume fine and coarse ash suggests their exploitation in synergy with satellite thermal infrared radiometer and ground-based microwave radar observations.

© 2012 Elsevier Inc. All rights reserved.

### 1. Introduction

The prompt detection of explosive volcanic eruptions and accurate determination of eruption-column altitude and ash-cloud movement are critical factors in the mitigation of volcanic risks to aviation and in the forecasting of ash fall on nearby communities (Prata et al., 1991; Sparks et al., 1997). On the one hand, civil prevention and protection procedures can be effectively activated if early warning is emitted in due time when quantitative information about volcanic explosions

is available to the decision makers (Tupper et al., 2007). On the other hand, volcanic ash transport and fallout models are used to mitigate the hazards posed by volcanic ash, but their practical use requires, in addition to adequate computing power, estimates of eruption source parameters (Bonadonna & Houghton, 2005; Sparks, 1986; Stohl et al., 2011). These parameters, which can be typically estimated in near real-time by visual inspection (if possible) and seismic measurements, include the eruption onset time, volcanic cloud altitude and explosive activity duration (Vogfjörð et al., 2005). Other volcanic source factors, such as the vertical distribution of ash mass and ash particle size distribution, are not easily retrievable during the eruption phase due to difficulty of direct probing and intrinsic microphysical variability (Stewart et al., 2008). Satellite remote sensing techniques can be exploited for this purpose, using thermal infrared channels available on both Low Earth Orbit (LEO) and Geostationary Earth Orbit (GEO) satellites (Gangale et al., 2010;

\* Corresponding author at: Department of Information Engineering (DIET), Sapienza University of Rome, Rome, Italy. Tel.: +39 06 44585406; fax: +39 06 44585918.

E-mail addresses: [frank.marzano@uniroma1.it](mailto:frank.marzano@uniroma1.it), [marzano@diet.uniroma1.it](mailto:marzano@diet.uniroma1.it) (F.S. Marzano), [mirko.lamantea@uniroma1.it](mailto:mirko.lamantea@uniroma1.it) (M. Lamantea), [mario.montopoli@univaq.it](mailto:mario.montopoli@univaq.it) (M. Montopoli), [herzog@unicam.ac.uk](mailto:herzog@unicam.ac.uk) (M. Herzog), [hans.graf@unicam.ac.uk](mailto:hans.graf@unicam.ac.uk) (H. Graf), [cimini@imaa.cnr.it](mailto:cimini@imaa.cnr.it) (D. Cimini).

Wen & Rose, 1994). Due to the strong optical extinction of ash cloud top layers, optical and infrared spaceborne imagery can provide a good estimate of the fine ash cloud coverage, but a less accurate estimate of its concentration and columnar content affected by the possible presence of ice particles and aggregates (e.g., Yu et al., 2002).

Microwave weather scanning radars have been successfully used to provide basic eruption observations in the last three decades, even though initially only qualitative description of eruption features have been provided through the analysis of radar reflectivity measured fields (Lacasse et al., 2004; Harris & Rose, 1983; Rose et al., 1995). To this aim single-polarization Doppler radars from L-band to K-band have been also employed (Gouhier & Donnadieu, 2008; Hort et al., 2003). More recently, by exploiting the well established techniques used for physically-based radar remote sensing of rainfall, the weather radar backscattered power has been used to derive quantitative estimates of volcanic eruptive mass, ash fallout and ash size category (Marzano et al., 2006b, 2010a, 2011). The inversion of microwave radar measurements of ash clouds, called Volcanic Ash Radar Retrieval (VARR) algorithm, is founded on a physically-based forward reflectivity model coupled with a Bayesian classification and regression retrieval of ash concentration and fallout intensity (Marzano et al., 2006a). The VARR approach has been also combined with the outputs of a microphysical mesoscale volcanic eruption model and extended to deal with non-spherical ash particles using X-band dual-polarized radars (Marzano et al., 2010b, 2012a).

Within the physical–statistical assumptions of the radar forward model and the sensitivity of the observing instrument, the Bayesian VARR technique represents an effective methodology to detect and estimate near-source volcanic plume features. The VARR methodology has been already applied to extract ash cloud features in several recent eruptions, characterized by the availability of a nearby weather radar: i) the Grímsvötn Icelandic volcano eruption on 2004, using a C-band weather radar (Marzano et al., 2010a); ii) the Augustine volcano eruption on 2006 in Alaska, analyzed using S-band weather radar imagery (Marzano et al., 2010b, 2012b); iii) the recent explosive eruption of the Eyjafjöll Icelandic volcano on 2010, using C-band radar data and an improved VARR technique (Marzano et al., 2011); and iv) the Mt. Etna eruption on 2011 in Italy, observed from a mobile X-band dual-polarization radar (Vulpiani et al., 2011). The main VARR assumptions are based on the statistical characterization of ash characteristics in terms of particle size distribution, fall velocity, physical and dielectric properties and the number of ash categories that can be discriminated using radar data.

The major volcanic parameters, derived from the time series of radar data three-dimensional (3D) volumes, are basically the distribution of ash concentration and fallout with a spatial resolution depending on the radar schedule (e.g., between few hundreds of meters to few kilometers) and a time resolution of few minutes. From this geophysical retrieval within an area of a hundred of square kilometers around the volcano vent, both total ash volume and mass due to the eruption event together with near-surface ash load, maximum height of volcanic cloud and eruption discharge rate can be obtained (Marzano et al., 2011). It should be pointed out that, depending on the distance and the radar sensitivity, for the 2011 Grímsvötn case study VARR ash products basically include coarse ash and lapilli fallout, whereas fine ash particles are generally not detected. However, the latter represents only a small fraction of the total erupted volume, even though the fine ash plume can be dispersed very far from the vent (Wen & Rose, 1994).

The present work is devoted to the description and discussion of new results of VARR methodology, for the first time applied to the recent sub-glacial Plinian explosive eruptions of Icelandic Grímsvötn volcano, whose maximum activities occurred in May 2011 (Showstack, 2011). The 2011 Grímsvötn eruption has been monitored and measured by the Keflavík C-band weather radar at a distance of about 260 km from the volcano vent in the same way to the eruption of 2004. The

prevailing southerly winds stretched the plume toward the Arctic pole, thus preventing the ash plume to move toward continental Europe and threatening the airline traffic. This fortunate circumstance is probably the reason for the reduced interest of the international community for the 2011 Grímsvötn eruption with respect to the 2010 Eyjafjöll one (Stohl et al., 2011). The sub-Plinian ash cloud in Eyjafjöll was persistent and fine-grained, while the ash in Grímsvötn was coarser and not as dangerous as for Eyjafjöll since it fell to the ground faster. Radar-based ash retrieval results for the Grímsvötn eruption cannot be compared with ground measurements due to the lack, so far, of ash loading sampling and drills, but they have been qualitatively and quantitatively compared with available satellite microwave radiometric imagery. The latter represents an appealing technique to extract an estimate of ash cloud concentration, even though its operational use is limited by the low temporal repetition typical of the LEO platforms (Delene et al., 1996).

The paper is structured as follows. In Section 2 the 2011 Grímsvötn eruption is described together with available radar imagery and a short description of the main VARR features. In Section 3 weather radar retrievals in terms of space–time volcanic cloud products are presented, discussed and compared. Section 4 is aimed at showing complementary remote sensing data, based on spaceborne microwave radiometer measurements, in order to corroborate radar-based ash estimates as ground ash-loading samples are not available yet. Section 5 is dedicated to the conclusions and future perspectives.

## 2. Grímsvötn volcano eruption on 2011

The 2011 Grímsvötn volcano eruption and the available weather radar data at C-band are illustrated and discussed in the following paragraphs.

### 2.1. Eruption description

The 2011 eruption of the Grímsvötn volcano, located in the north-west of the Vatnajökull glacier in south-east Iceland (see Fig. 1 panel e) that is one of Iceland's most active volcanoes, started on the afternoon of May 21, 2011. The Grímsvötn eruption on May 2011 was the largest eruption in Iceland within the last hundred years (Thordarson & Larsen, 2007). The eruption plume rose to an altitude even higher than 15 km, thus representing a unique Plinian sub-glacial eruption, as shown in the amazing pictures of Fig. 1 panels c) and d). Initially, the plume drifted to the south-east and subsequently to the north, as suggested by the MODIS (Moderate-resolution Imaging Spectroradiometer) images of Fig. 1 panel a), observed from the Aqua platform at 1 km resolution on May 22, 2011 at 05:15 UTC (Universal Time Coordinate) and panel b), observed from the Terra platform at 1 km resolution on May 22, 2011 at 13:00 UTC. As mentioned, the eruption caused some impairments to air travel in Iceland and north-western Europe from 22 to 25 May 2011.

Before May 2011, the last eruption of Grímsvötn was in 2004, with the previous most powerful eruptions in 1783, 1873 and 1902 (Larsen et al., 1998). Indeed, eruptions are relatively common in the Grímsvötn area, occurring once every 10 years and they are usually short and localized. Anyhow, the past volcanic events in this area have been connected to devastating eruptions located at the same fissure (e.g., during the dreadful Laki eruption in 1783 an eruption was ongoing also at Grímsvötn which continued to erupt until 1785). The Grímsvötn area consists of a series of sub-glacial lakes that are never completely frozen due to the volcanic activity below them. Because most of the Grímsvötn volcano lies underneath the Vatnajökull glacier, most of its eruptions have been subglacial and the interaction of magma and meltwater from the ice causes phreato-magmatic explosive activity. The main risk, arising from eruptions in the area, is a phenomenon known in Icelandic as *jökulhlaup* (i.e., glacial outburst

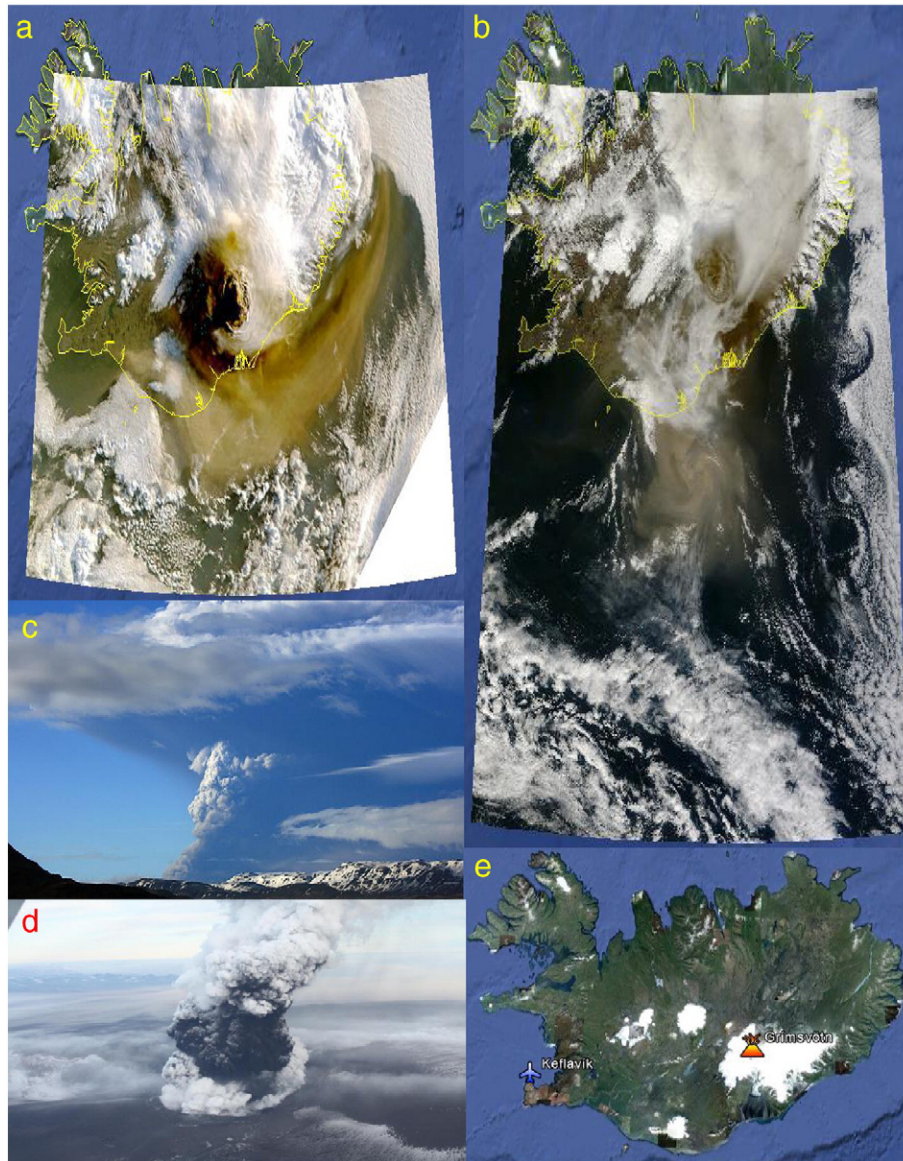


**Fig. 1.** (Panel a) Image of geolocated MODIS aboard the Aqua satellite, taken over Iceland at 1 km resolution on May 22, 2011 at 05:15 UTC (courtesy Jeff Schmaltz of MODIS Rapid Response Team at NASA GSFC and Google Earth – Europa Technologies, Data SIO, NOAA, U.S. Navy, NGA, GEBCO); (panel b) image of geolocated MODIS aboard the Terra satellite, taken over Iceland at 1 km resolution on May 22, 2011 at 13:00 UTC (courtesy Jeff Schmaltz of MODIS Rapid Response Team at NASA GSFC and Google Earth – Europa Technologies, Data SIO, NOAA, U.S. Navy, NGA, GEBCO); (panel c) the eruption column, as seen over the Grímsvötn volcano on May 21, 2011 around 22:00 UTC (courtesy AP Photo/Halldóra Kristín Unnarsdóttir); (panel d) aerial view of Grímsvötn volcano eruption column on May 24, 2011 (courtesy of Magnús Tumi Guðmundsson, University of Iceland); and (panel e) map of Iceland where the Grímsvötn volcano, the Keflavík radar site and the typical Iceland icecap are shown (courtesy of Google Earth – Europa Technologies, Cnes/Spot Image, Data SIO, NOAA, U.S. Navy, NGA, GEBCO).

floods). In other words the water, trapped under the ice in the lakes, bursts out due to the eruption with extreme violence, causing a powerful and extremely dangerous outburst of water. As a matter of fact, in 1996 the Grímsvötn eruption in the area caused a peak flow of  $50,000 \text{ m}^3 \text{ s}^{-1}$  of water runoff and lasted for several days.

Following the Iceland Meteorological Office (IMO) status reports, the 2011 Grímsvötn eruption is estimated to have started under the glacier around 17:30 UTC on May 21, 2011 when an intense spike in tremor activity was detected. At around 19:00 UTC, the eruption broke the ice cover of the glacier and started spewing volcanic ash into the air. The eruption plume height quickly rose to about 20 km, accompanied by a series of small earthquakes. During May 22 the ash plume fell to around 10 km altitude, rising occasionally to 15 km. On May 23 the eruption was releasing more than 2000 tons of ash per second, totaling 120 million tons in the first 48 h.

On May 25 the Iceland Met Office confirmed the eruption had paused at 02:40 UTC and that the volcanic activity appeared to have stopped. At 15:00 the IMO issued an update stating that no further ash plume was expected. However there were still pulsating explosions producing ash and steam clouds, some reaching a few kilometers in height, rising up from the vent. There was still widespread ash in cloud layers up to 5 km from the eruption site. On May 26 IMO and the University of Iceland reported that ashfall was only occurring adjacent to the eruption site. Visual observations indicated that little ice meltwater was produced during the eruption so that the expected jökulhlaup did not occur. The 2011 Grímsvötn eruption officially ceased at 07:00 UTC on May 28, 2011 and, in terms of the Volcanic Explosivity Index (VEI), qualified as at least of class 4 (VEI-4), releasing more ash in the first 24 h than Eyjafjöll released during its entire 2010 eruption.

## 2.2. Radar data

The measured radar backscattered power, from a volume bin at range  $r$ , zenith angle  $\theta$  and azimuth angle  $\varphi$ , is proportional to the measured co-polar horizontally-polarized reflectivity factor  $Z_{Hm}$  (typically expressed in  $\text{mm}^6 \text{m}^{-3}$  or in dBZ). The volume bin ( $V_b$ ) is the minimum portion of atmosphere that can be detected by the transmitted radar beam and it can be approximated as  $V_b = (\pi/4) r^2 \Delta\theta \Delta\varphi \Delta r$ , where  $\Delta\theta$ ,  $\Delta\varphi$  and  $\Delta r$  are the elevation, azimuth and range resolution, respectively (Sauvageot, 1992).  $Z_{Hm}$  can be directly related to microphysical particle parameters. Under the Rayleigh scattering assumption, the radar wavelength is supposed to be larger than the particle sizes and for an ensemble of ash spherical particles the measured  $Z_{Hm}$  is equal to the sixth moment of the particle size distribution (Sauvageot, 1992). If the Rayleigh hypothesis does not hold, then the Mie scattering needs to be taken into account (e.g., Marzano et al., 2006a, 2010b). The more general solution for the Mie scattering problem, which includes the particle shape dependence, can be taken into account as well using the T-matrix numerical solution. The latter is useful for characterizing dual-polarization radar system once opportunely adapted for ash particles (Marzano et al., 2012a; Vulpiani et al., 2011).

The 2011 eruption was detected and monitored during its whole life span by the single polarization C-band (6 GHz, 5 cm wavelength) weather radar in Keflavík, located 260-km north-westwards away from the caldera of Grímsvötn volcano (see Fig. 1, panel a). Specifications of the Keflavík C-band radar are detailed elsewhere (Lacasse et al., 2004; Marzano et al., 2006b; Vogfjörð et al., 2005). The Keflavík C-band radar volumes were available from the IMO every  $\Delta t_s = 5$  min during the event from May 21, 2011 at 19:50 UTC till May 28, 2011 at 23:55 UTC. The radar dataset consists of a total of  $N_s = 2053$  volumes in spherical coordinates with 10 elevation angles, 420 azimuth angles and 260 range bins, the latter having a range width of about  $\Delta r = 2$  km and an azimuth and an elevation sampling of  $\Delta\varphi = 0.857^\circ$ ,  $\Delta\theta = 1^\circ$ , respectively. A 2-km radial average of measured radar returns has been performed to increase the minimum detectable reflectivity (MDZ) to about  $-3$  dBZ around the 260-km range around the Grímsvötn volcano vent. Only five elevation angles are considered here (specifically, at  $0.5^\circ$ ,  $0.9^\circ$ ,  $1.3^\circ$ ,  $2.4^\circ$  and  $3.5^\circ$ ) among those routinely available (note that, at 260 km from the radar and an elevation angle of  $3.5^\circ$ , for a standard atmosphere the estimated maximum detectable radar height is 20 km).

Eight of the most significant PPI (Plan Position Indicator) and RHI (Range Height Indicator) images of the measured radar reflectivity  $Z_{Hm}$  (expressed in dBZ, as usual), recorded on May 22, 2011 from 00:00 UTC till 21:00 UTC, are shown in Figs. 2 and 3, respectively. PPI horizontal images are acquired at  $0.9^\circ$  elevation angle, whereas RHI vertical sections are referred to the line connecting the volcano vent and the radar antenna (with respect to the north it corresponds to an azimuth of about  $80^\circ$ ). Environmental clutter signature was present for ranges close to the radar site and it has been removed during the data pre-processing. Moreover, some C-band interfering signals were also visible in the PPI imagery in terms of radial strips within PPI images and then properly removed. In RHI and PPI images the volcano vent is represented by a triangle. The lower portion of the ash plume between the volcano vent and 5.5 km is not detectable by the Keflavík radar due to the curvature of the microwave rays caused by atmospheric effects and the distance of the radar antenna from the vent itself, observed at elevation angles not lower than  $0.5^\circ$  (see Fig. 3). The ash plume increases its spatial distribution as the strength of the eruption increases between 3:00 and 6:00 UTC on May 22. From RHI imagery the upper height of the ash cloud, as detected by

the weather radar, is above 18 km. The PPI images show that the ash mass movement is mostly toward north. Radar reflectivity factor  $Z_{Hm}$  values are up to 50 dBZ in correspondence to the peak of the ash plume height.

## 3. Radar remote sensing retrieval

The results of the VARR algorithm, applied to radar data gathered during the Grímsvötn volcano eruption, are illustrated and discussed in the following paragraphs by considering the following parameters of volcanological interest: mass concentration, maximum height of the ash cloud, total mass and volume, eruption discharge rate (EDR) and spatial ash distribution. A brief introduction to VARR methodology will be also provided.

### 3.1. VARR methodology

The VARR technique is extensively described in previous works (Marzano et al., 2006b, 2010a,b) and mentioned as possible operational tool in the ESA-EUMETSAT proceeding (Zehner, 2010).

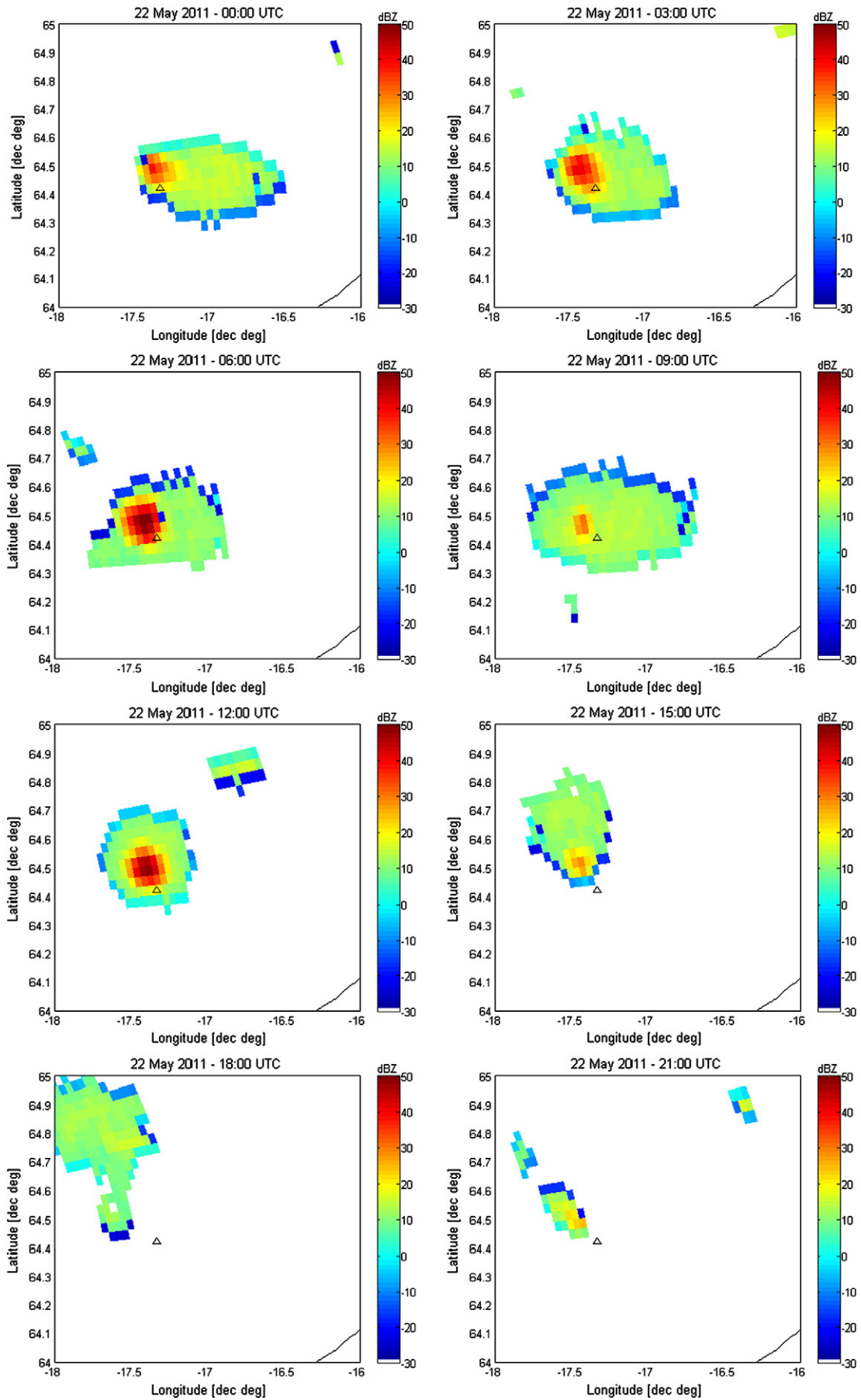
For convenience and completeness, the VARR major features are summarized here. As most geophysical remote sensing problems, the radar-based retrieval of ash plumes belongs to the class of ill-posed problems (Rodgers, 2000). In order to regularize an ill-posed problem, one has to introduce more measurements and/or a priori assumptions which may be incomplete, but must be explicit. For physically-based inversion approaches, this a priori information can be derived from the underlying microphysical-electromagnetic model.

The VARR methodology for Doppler single-polarization weather radars belongs to the physically-based retrieval algorithm category and is organized in 2 basic steps: i) ash classification and ii) ash estimation. Both steps are trained by a physical-electromagnetic forward model, characterized by spherical particle size distribution (PSD) of ash species and a radar backscattering model. PSD is usually modeled as a scaled Gamma PSD whose main parameters are the number concentration  $N_n$ , number-weighted diameter  $D_n$ , and the shape parameter  $\mu$ ; all these parameters are treated as random variables and constrained by a priori (experimental and physical) information.

In order to optimize and adapt the retrieval algorithm to the Icelandic scenario, in a previous work VARR has been statistically calibrated through ground-based PSD samples, taken within the Vatnajökull ice cap in 2005 and 2006 after the Grímsvötn last eruption occurred in 2004 (Oddsson et al., 2008, 2012). The ground ash samples have been subdivided into  $N_c = 9$  ash classes and, within each class, a Gaussian random distribution has been assumed for: i)  $D_n$  with average value  $\langle D_n \rangle$  equal to 0.006, 0.0641 and 0.5825 mm for fine, coarse and lapilli ash, respectively, a standard deviation  $\sigma_{D_n} = 0.2 \langle D_n \rangle$  and a corresponding variability of  $0.001 \leq D_n < 0.06$  mm,  $0.06 \leq D_n < 0.5$  mm, and  $0.5 \leq D_n \leq 7.0$  mm; and ii) ash concentration  $C_a$  with mean value  $\langle C_a \rangle$  equal to 0.1, 1 and  $5 \text{ g m}^{-3}$  for light, moderate and intense concentration regimes, respectively, and a standard deviation  $\sigma_{C_a} = 0.5 \langle C_a \rangle$ . The ash density  $\rho_a$  has been put equal to an average value of  $1200 \text{ kg m}^{-3}$ , typical of Icelandic basaltic phreatomagmatic tephra as estimated after the 2004 Grímsvötn eruption (Oddsson et al., 2008, 2012). The optimal PSD shape parameter  $\mu$  has been set to 0.9, 1.1 and 1.4 for fine, coarse and lapilli particles. The features of the 9 ash classes are summarized in Table 1.

Ash class discrimination with respect to average diameter  $\langle D_n \rangle$  and average ash concentration  $\langle C_a \rangle$  implies the capability of classifying the radar volume reflectivity measurements into one of  $N_c$  classes. Ash classification is performed by means of Maximum-A-Posteriori

**Fig. 2.** Eight of the most significant PPI (Plan Position Indicator, horizontal projection) radar images at  $0.9^\circ$  elevation angle (corresponding to a height of about 8 km above the volcano vent; see Fig. 3 as well) showing the recorded Keflavík C-band radar reflectivity on May 22, 2011 from 00:00 UTC till 21:00 UTC. See text for details.



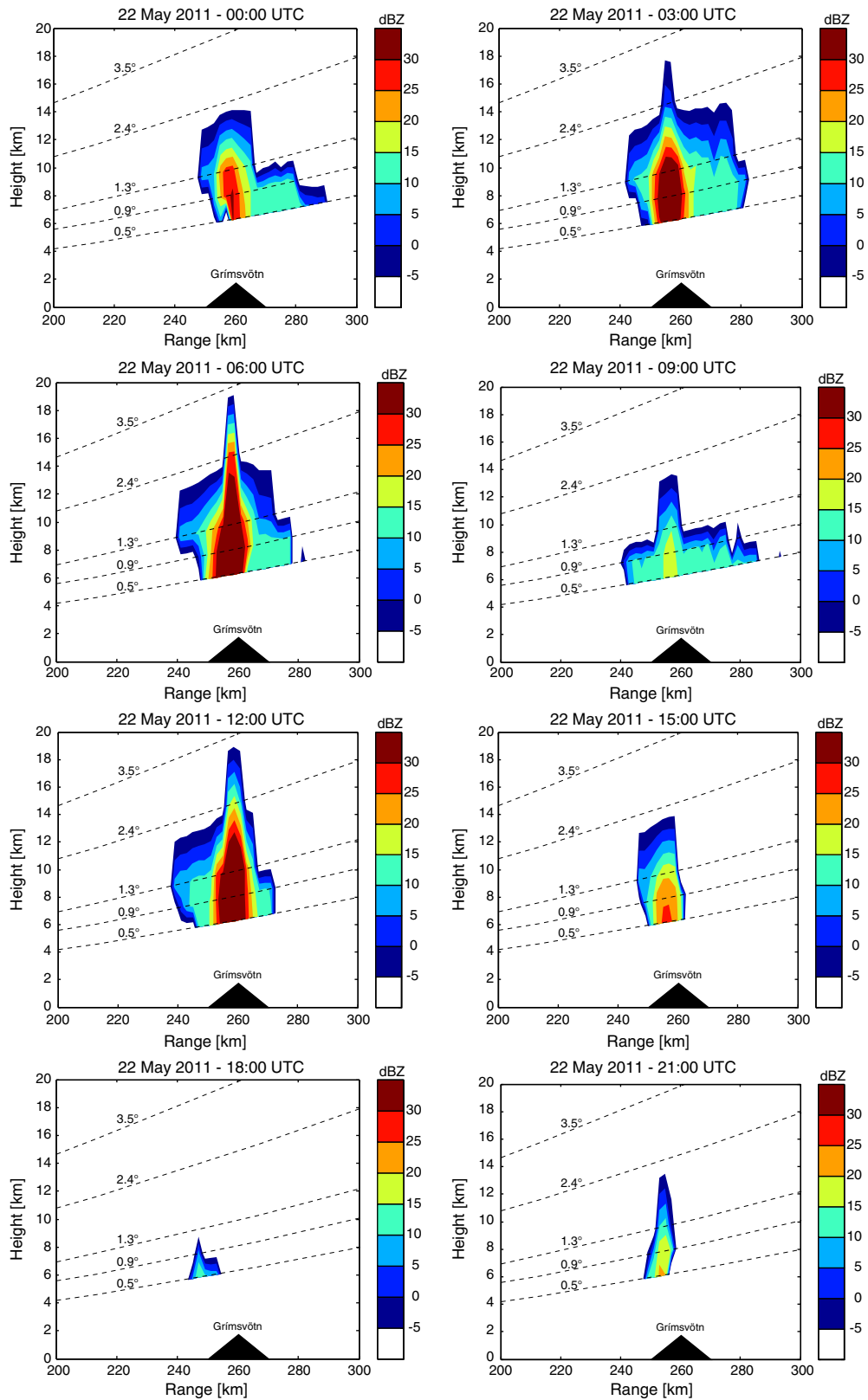


**Fig. 3.** Eight of the most significant RHI (Range Height Indicator) radar images showing the recorded Keflavik C-band radar reflectivity on May 22, 2011 from 00:00 UTC till 21:00 UTC. See text for details.

probability (MAP) estimation. The probability density function (PDF) of each ash class  $c$ , conditioned to the measured copolar reflectivity factor  $Z_{Hm}$  can be expressed through the Bayes theorem. The MAP

estimation of ash class,  $c$ , corresponds to the maximization with respect to  $c$  of the posterior PDF  $p(c|Z_{Hm})$ . Under the assumption of multivariate Gaussian PDFs, the MAP maximization reduces to the

**Table 1**  
Microphysical characterization of 9 ash classes in terms of average ash diameter  $\langle D_n \rangle$  and concentration  $\langle C_a \rangle$ . The variability within each class is Gaussian with a deviation proportional to the mean,  $\sigma_{Dn} = 0.2 \langle D_n \rangle$  and  $\sigma_{Ca} = 0.5 \langle C_a \rangle$ .

Ash classes	Light concentration $\langle C_a \rangle = 0.1 \text{ g m}^{-3}$	Moderate concentration $\langle C_a \rangle = 1.0 \text{ g m}^{-3}$	Intense concentration $\langle C_a \rangle = 5.0 \text{ g m}^{-3}$
Fine ash $\langle D_n \rangle = 0.006 \text{ mm}$	FA-LC class = 1	FA-MC class = 2	FA-IC class = 3
Coarse ash $\langle D_n \rangle = 0.064 \text{ mm}$	CA-LC class = 4	FA-MC class = 5	CA-IC class = 6
Lapilli $\langle D_n \rangle = 0.583 \text{ mm}$	LP-LC class = 7	LP-MC class = 8	LP-IC class = 9

following minimization which provides an ash class  $c$  for a given volume bin centered in  $(r, \theta, \varphi)$  (Marzano et al., 2006b):

$$\hat{c}(r, \theta, \varphi) = \text{Min}_c \left\{ \frac{[Z_{Hm}(r, \theta, \varphi) - m_z^{(c)}]^2}{(\sigma_z^{(c)})^2} + \ln(\sigma_z^{(c)})^2 - 2 \ln p[c(r, \theta, \varphi)] \right\} \quad (1)$$

where  $\text{Min}_c$  is the minimum value with respect to  $c$ ,  $m_z^{(c)}$  and  $\sigma_z^{(c)}$  are the reflectivity mean and standard deviation of ash class  $c$ , whereas  $p(c)$  is the a priori PDF of ash class  $c$  and the ash class perturbations have been assumed uncorrelated. Computing Eq. (1) requires knowledge of the reflectivity mean ( $m_z^{(c)}$ ) and standard deviation ( $\sigma_z^{(c)}$ ) of each ash class,  $c$ , derived from the 9-class simulated synthetic data set, previously described.

For each radar volume bin, the ash fallout rate  $R_a$  [ $\text{kg m}^{-2} \text{ s}^{-1}$ ] and ash concentration  $C_a$  [ $\text{g m}^{-3}$ ] can be theoretically expressed by means of the terminal ashfall velocity  $v_a(D)$ , and the ash mass particle  $m_a$ , respectively whereas the ash mass particle is typically approximated by an equivalent sphere (Marzano et al., 2006b). A power-law dependence of  $v_a$  on  $D$  is usually assumed (Wilson, 1972; Wilson et al., 1978). The inversion problem to retrieve  $C_a$  and  $R_a$  from  $Z_{Hm}$  is ill-posed so that it can be statistically approached (Rodgers, 2000). Through the training forward model, a power-law regressive approximation may be used as a function of the ash class  $c$  for both  $C_a$  and  $R_a$  for a given volume bin centered in  $(r, \theta, \varphi)$  (Marzano et al., 2006b):

$$\begin{cases} R_a^{(c)}(r, \theta, \varphi) = c_c Z_{Hm}^{d_c}(r, \theta, \varphi) \\ C_a^{(c)}(r, \theta, \varphi) = a_c Z_{Hm}^{b_c}(r, \theta, \varphi) \end{cases} \quad (2)$$

where  $r$  is the range,  $\theta$  is the elevation and  $\varphi$  is the azimuth angle, whereas  $Z_{Hm}$  is the measured reflectivity factor and  $a_c$ ,  $b_c$ ,  $c_c$  and  $d_c$  are the regression coefficients, derived from simulated training dataset for each ash class  $c$ .

Weather radar observations exhibit a sensitivity to ash size and concentration mainly dependent on the transmitted wavelength, receiver minimum detectable signal and range (received power is inversely proportional to square range). By considering a MDZ signal of about  $-3$  dBZ, as in the case of the Keflavik around the Grímsvötn vent, numerical analyses have shown that intense concentration of fine ash (about  $5 \text{ g m}^{-3}$  of average diameter of  $0.01 \text{ mm}$ ) cannot be detected by a C-band radar (Marzano et al., 2006b). This means that radar measurements can be used, in the considered event, to detect only light to intense concentration of coarse ash and any lapilli distribution. Other major critical issues are: i) conical observation geometry inevitably produces occluded regions at longer ranges and in the presence of obstacles (e.g., a mountain or even the vent). Techniques for the reconstruction of the reflectivity vertical profile may be devised (Marzano et al., 2012b); ii) the radar ash detectability is depending not only on the receiver sensitivity, but also quadratically on the inverse distance so that only larger particles can produce a radar signature at longer ranges; iii) due to the centimeter wavelength, fine ash is hardly detected by reflectivity measurements (in the Rayleigh scattering regime the latter inversely depends on the

fourth power of wavelength) so that most microwave radar signatures refer to near-source plume depending on the sedimentation and settling of coarse ash and lapilli. Indeed, fine ash represents few percentage of the total tephra and can be transported far from the volcano vent (Wen & Rose, 1994); iv) the discrimination between ash and hydrometeor and the identification of ash-water aggregates is beyond the current capabilities of single-polarization weather radar and should be treated as an ambiguity (uncertainty) affecting the qualitative and quantitative interpretation of the radar imagery of ash clouds (Marzano et al., 2010a,b); v) for ash monitoring below Ku band (12–18 GHz), the specific attenuation, due to fine and coarse particle and gas absorption along the beam, is usually lower than  $1 \text{ dB km}^{-1}$ , but it can largely increase above Ku band (Marzano et al., 2006a). vi) At longer ranges (longer than  $120 \text{ km}$ ) the radar volume bin may have a transverse cross-section larger than few kilometers (the radial resolution is governed by the pulse width and can be as short as hundreds of meters). This may produce some ash content underestimation due to the non-uniform antenna beam filling as experienced for rainfall clouds (e.g., Kitchen & Jackson, 1993).

Some of the above limitations may be overcome by using polarimetric measurements and using higher frequency systems in order to increase the radar sensitivity to ash (Marzano et al., 2012a). But even with dual-polarized radars, the particle state is difficult to discriminate between coexistence or aggregation of ash and hydrometeors, even though the partial beam blockage and beam-filling errors may be reduced using the differential phase measurements (e.g., Zrníc & Ryzkov, 1996). Moreover, at higher frequencies the path attenuation can become a further problem to deal with (Marzano et al., 2006a). Eventually, the performances of the polarimetric VARR algorithm will be affected by the accuracy and completeness of the polarimetric model of ash radar response. Many of the above errors might be corrected with ancillary information (e.g., satellite data, synergy with lidar, ceilometers and camera systems) which are not always available with the same space–time resolution of a scanning radar. In order to deal with these uncertainties, we can estimate them in terms of error average and variance and introduce this variability into our modeled noise. This is a conservative choice as the estimate standard deviation will increase, but it is a rigorous way to introduce this lack of knowledge within our Bayesian inversion algorithm. On the other hand, any advancement in the understanding of the observed ash clouds can be, in principle, incorporated within the forward model of the physically-based VARR technique in order to improve its validity and reduce its uncertainty.

### 3.2. Time series products

The instantaneous volcanic ash cloud volume  $V_{ac}(t)$  [ $\text{m}^3$ ], which represents the detected volume of the ash cloud at a given nominal time step  $t$ , can be estimated by using a threshold  $C_{ath}$  on the estimated concentration  $C_a(r, \theta, \varphi)$  through Eq. (2) at a given position  $(r, \theta, \varphi)$  with respect to the radar antenna. However, as already noted in Fig. 3, the total portion of the ash cloud  $V_{ac}(t)$  is not detectable by the scanning radar, thus inducing an underestimation of the total ash volume and mass due to the radar observation geometry and the presence of partial obstructions along the ray paths. In order to partially overcome this problem, we have applied a simple reconstruction of the vertical

profile of reflectivity (VPR), based on the assumption of a reflectivity constant value, down to the surface, equal to the lowest measured reflectivity  $Z_{Hm}$  (Marzano et al., 2012b). The drawback of this approach is a possible overestimation of the ash mass in case the concentration is increasing with height and vice versa. However, in order to produce an overall estimate of the total erupted mass, previous results show that this VPR correction leads to better results than assuming no ash at all below the radar-based minimum height (Marzano et al., 2012b). Using  $V_{ac}(t)$ , the instantaneous airborne ash mass  $M_a(t)$  [kg], can be estimated from each radar volume by:

$$M_a(t) = \int_{V_{ac}(t)} C_a(r, \theta, \phi, t) dV = \rho_a V_a(t). \quad (3)$$

The instantaneous eruption airborne ash volume  $V_a(t)$  [m<sup>3</sup>] can be obtained from the previous equation where  $\rho_a$  is the ash density, assumed to be space–time constant within the ash cloud and equal to about 1200 kg m<sup>-3</sup>.

The deposited ash at ground during the eruption event can be estimated from the retrieved ash fall rate  $R_a$ , estimated in Eq. (2) from radar measurements. By indicating with  $R_{as}(\rho, \varphi, t)$  the instantaneous ash fall rate reconstructed through VPR at the surface and expressed in surface polar coordinates  $(\rho, \varphi)$  with respect to the radar site (i.e.,  $R_{as}(\rho, \varphi, t)$  is equal to  $R_a(r, \theta, \varphi, t)$  when the antenna elevation angle  $\theta$  is zero or the minimum allowed), the spatial distribution of the radar-derived instantaneous deposited tephra mass loading or depth  $D_a(\rho, \varphi)$  [kg m<sup>-2</sup>] within the whole volcanic eruption duration can be expressed by:

$$D_a(\rho, \varphi) = \int_{t_i}^{t_f} R_{as}(\rho, \varphi, t) dt \quad (4)$$

where  $t_i$  and  $t_f$  are the initial and final time steps of the volcanic eruption. By assuming a constant eruption activity within the time sampling interval  $\Delta t$  (in our case equal to 5 min), the radar-derived instantaneous tephra mass  $M_{as}(t)$  [kg], deposited at the surface within the whole ash fall area  $S_a$ , can be derived from:

$$M_{as}(t) = \Delta t \int_{S_a} R_{as}(\rho, \varphi, t) dS = V_{as}(t) \rho_a \quad (5a)$$

where  $dS$  is the ground-projected pixel of radar-based estimates (in our case equal to about  $2 \times 2$  km<sup>2</sup> in a Cartesian grid). The corresponding ash volume  $V_{as}(t)$  [m<sup>3</sup>] of the deposited tephra is obtained from  $M_{as}(t)$  through Eq. (5a). We can also evaluate the total space–time deposited tephra mass  $M_{aT}$  [kg] within the whole eruption duration by using:

$$M_{aT} = \int_{S_a} D_a(\rho, \varphi) dS = V_{aT} \rho_a \quad (5b)$$

where  $V_{aT}$  is the radar-derived total ash volume of the detected erupted cloud. Thus, the detected total eruption ash volume  $V_{aT}$  [m<sup>3</sup>] is obtained from  $V_{aT} = M_{aT} / \rho_a$ .

The temporal trend of the ash volume  $V_{as}(t)$ , retrieved from VARR, is shown in Fig. 4 using all available data from May 21, 2011 at 19:50 UTC till May 23, 2011 at 23:55 UTC which is the most significant time interval of the 2011 Grímsvötn eruption. Correspondingly, the total mass  $M_{as}(t)$  at each time step  $t$  is shown in Fig. 5 for the same time windows as in Fig. 4. These figures confirm the qualitative description of the Grímsvötn eruption in Section 2.1 and the Plinian features of this imponent eruption. The period between the end of May 21 and the beginning of May 22 was the most intense with an initial peak of the total ash volume of about  $2.8 \times 10^6$  m<sup>3</sup> (and a peak ash mass of about  $3.3 \times 10^9$  kg from Fig. 5), followed by an intermittent decreasing eruption activity till afternoon of May 22. After a short

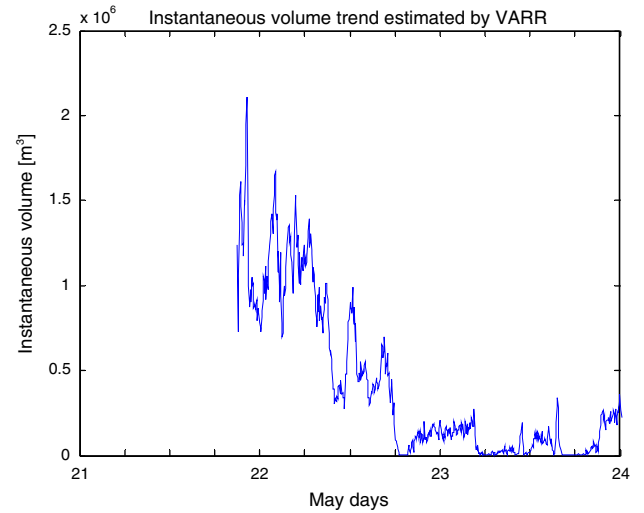


Fig. 4. Instantaneous deposited ash volume  $V_{as}(t)$  versus time expressed in terms of scan days from May 21, 2011 at 19:50 UTC till May 23, 2011 at 23:55 UTC. The ticks on the x-axis have a spacing equal to 6 h. The scan sampling period is equal to 5 min.

pause a cycle of 3 new eruptions of medium intensity with erupted total volumes between  $0.5 \times 10^6$  and  $0.75 \times 10^6$  m<sup>3</sup> till midday of May 24. From May 24 till the end of May 28 the erupted volcanic activity has continued with a low intermittent ash production with level below  $0.3 \times 10^6$  m<sup>3</sup>.

The spatial distribution of the instantaneous maximum plume height  $H_a(\rho, \varphi, t)$  [km], expressed in surface polar coordinates  $(\rho, \varphi)$  with respect to the radar site, can be derived by using either a threshold  $Z_{Hmth}$  on the measured reflectivity  $Z_{Hm}(r, \theta, \varphi, t)$  or a threshold  $C_{ath}$  on  $C_a(r, \theta, \varphi, t)$ . The plume maximum height  $H_{aM}(t)$  with respect to any  $(\rho, \varphi)$  can be also extracted once  $H_a(\rho, \varphi, t)$  is estimated. The analysis of the plume maximum height  $H_{aM}(t)$  is both an important input parameter within volcanological models and a crucial feature for aircraft routes planning in the areas near the volcanic eruption, as Plinian and sub-Plinian explosive eruptions can reach height peaks at the same altitude of modern commercial airplanes flights. It is worth reminding that the radar-based estimate of  $H_{aM}(t)$  suffers of lack of microwave visibility over the vent considering the available observation geometry (see Fig. 3). Moreover, spurious ground clutter can affect the plume height estimate in a given domain.

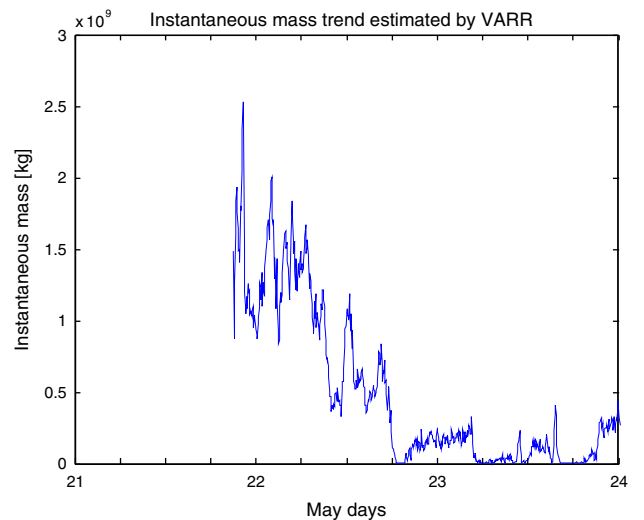


Fig. 5. As in Fig. 4, but for the instantaneous deposited ash mass  $M_{as}(t)$  versus time expressed in terms of scan days from May 21, 2011 at 19:50 UTC till May 23, 2011 at 23:55 UTC.

The temporal evolution of the maximum plume height  $H_{aM}$  is shown in Fig. 6 using the same data of Figs. 4 and 5 and applying the previously mentioned two different techniques. The detection thresholds  $Z_{Hmth}$  on reflectivity has been set to  $-3$  dBZ, whereas the ash concentration threshold  $C_{ath}$  to  $10^{-6}$  kg m $^{-3}$ . The choice of  $C_{ath}$  is a critical factor that requires a special attention. The  $C_{ath}$  value chosen in this work is a conservative choice with respect to the Civil Aviation Authority (CAA) that currently sets the volcanic ash tolerance level to a concentration of  $2 \times 10^{-6}$  kg m $^{-3}$  at regular cruise altitudes (typically any airspace with a larger ash concentration is generally classified as a no-fly zone). In case the radar volume did not show any value above the mentioned threshold, the  $H_{aM}$  estimate was labeled as void value (no data in the figure trend). Note that the trends shown in Fig. 6 are obtained considering for each time instant the maximum height values have been averaged by using a fixed-length moving window (in our case, equal to 25 min) in order smooth abrupt variations. Thus, RHI instantaneous trends can slightly differ from these estimates since RHI does not include any averaging.

The plume height estimation shows a certain variability, also due to the altitude discrete sampling of radar beams at given elevations. The maximum height is indeed higher than 18 km in correspondence of the peaks of  $V_{as}(t)$  till the morning of May 22, then decreases to about 15 km in the rest of the day and finally sets to altitudes less than 13 km for the following time. The temporal behavior of the 2 estimates of  $H_{aM}$  is quite similar with an intermittent behavior after the midday of May 24.

From the knowledge of the maximum plume height instantaneous retrievals  $H_{aM}(t)$  the eruption discharge rate (EDR) can be also estimated. EDR expresses the total ash volume per unit time and is a useful parameter to mark the intensity of a volcanic eruption and to characterize a volcanological eruption model. By exploiting the Morton relation (Morton et al., 1956), the estimated EDR  $Q_H(t)$  [m $^3$  s $^{-1}$ ] can be obtained from maximum plume height through an approximate relation which shows that EDR is proportional to the fourth power of the height (Oddsson et al., 2008, 2012):

$$Q_H(t) = a_Q [H_{aM}(t)]^4 \quad (6)$$

where  $a_Q = 0.085$  if  $H_{aM}$  is in km and  $Q_H$  in m $^3$  s $^{-1}$ . The power-dependence of  $Q_H(t)$  on height means that small fluctuations of the

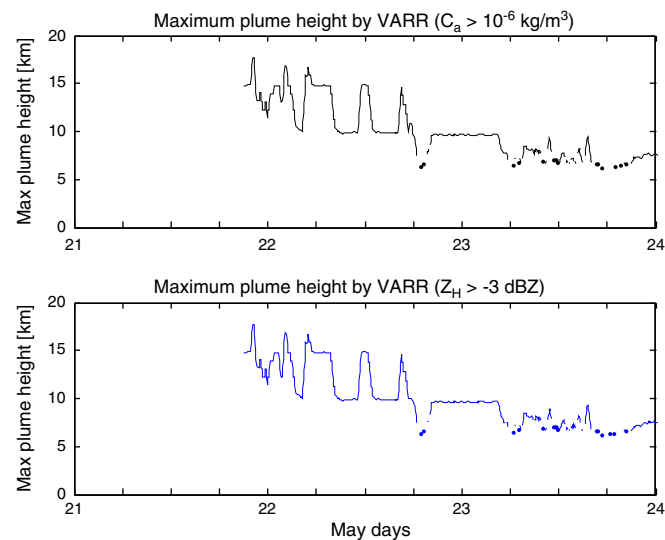


Fig. 6. As in Fig. 4, but for the instantaneous maximum plume height derived from VARR algorithm with (upper panel) reflectivity threshold ( $Z_H > -3$  dBZ) and (lower panel) concentration threshold ( $C_a > 10^{-6}$  kg m $^{-3}$ ) and smoothed over a 25 min (i.e. 5 radar acquisitions) sliding window. Void (no) values indicate no data above the threshold.

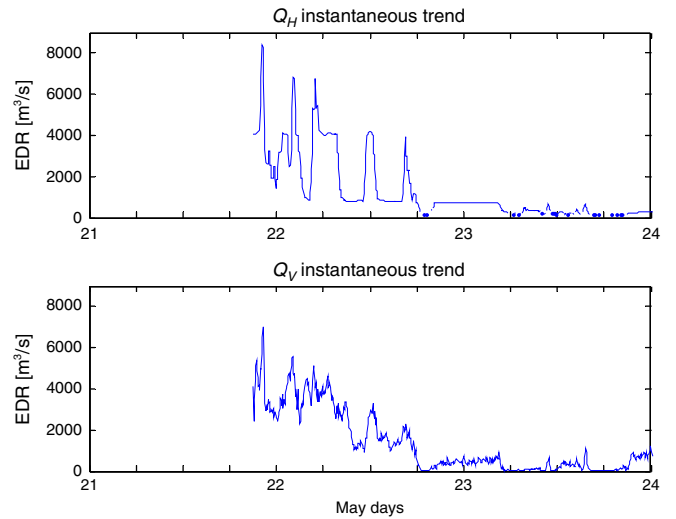


Fig. 7. As in Fig. 4, but for the instantaneous eruption discharge rate (EDR), obtained from: (top panel) the maximum plume height derived from VARR algorithm with concentration threshold ( $C_a > 10^{-6}$  kg m $^{-3}$ ); and (bottom panel) the rate of the instantaneous total ash volume  $V_a$ .

estimated height can cause large EDR variations. EDR temporal trends, obtained from VARR, using  $H_{aM}(t)$  with a threshold on ash concentration  $C_a$ , are shown in Fig. 7. As expected, the maximum height is reached when the volcanic eruption activity is the most intense during the first day.

The EDR can be also directly evaluated from the temporal trend of the estimated ash volume  $V_a(t)$ . The radar-derived EDR  $Q_V(t)$  [m $^3$  s $^{-1}$ ] is evaluated through the ratio between the temporal average airborne ash volume  $V_a(t)$  and the sampling interval  $\Delta t$ :

$$Q_V(t) = \frac{V_a(t)}{\Delta t} = \frac{1}{\rho_a \Delta t} \int_{V_{ac}(t)} C_a(r, \theta, \phi, t) dV \quad (7)$$

where the last equality is derived from Eq. (3). Fig. 7 shows  $Q_V(t)$ , with peaks of the order of  $9 \times 10^3$  m $^3$  s $^{-1}$ . The difference between the height-derived estimated  $Q_H(t)$  and the volume-derived estimated  $Q_V(t)$  can be explained by considering that  $Q_H$  is only depending on the ash cloud altitude, whereas  $Q_V$  is derived from the total erupted ash volume. Moreover, the retrieval of  $Q_H(t)$  is affected by the discrete number of available elevations, whereas the estimation of  $Q_V(t)$  is affected by the volume reconstruction through the VPR approach.

### 3.3. Spatial map products

From the near-surface retrieved ash fall rate  $R_a(\rho, \varphi, t)$  obtained by performing a VPR reconstruction, we can derive the spatial distribution of the radar-derived deposited tephra density or loading  $D_a(\rho, \varphi)$ , as shown in Eq. (4). The latter can be extracted from the time integral of  $R_a(\rho, \varphi, t)$  over the available time step by assuming an average constant eruption activity in that interval (of 5 min). The retrieved ash mass loading  $D_a(\rho, \varphi)$  is shown in Fig. 8 in correspondence of the time steps of Figs. 2 and 3. This figure confirms that coarse ash and lapilli are confined within a relatively small area around the volcano vent with values larger than 200 kg m $^{-2}$ .

The total erupted ash mass  $M_{aT}$  can be evaluated through the spatial integration of the instantaneous deposited tephra  $D_a(\rho, \varphi)$ , derived from VARR, as shown in Eq. (5). The total volume  $V_{aT}$  of the eruption event is then obtained from the estimated mass  $M_{aT}$  through the same equation. Table 2 shows the intercomparison results in terms of overall mass  $M_{aT}$  and volume  $V_{aT}$  as retrieved by means of VARR methodology. Note that, in order to provide an intrinsic variability of VARR estimates, estimations have been carried out

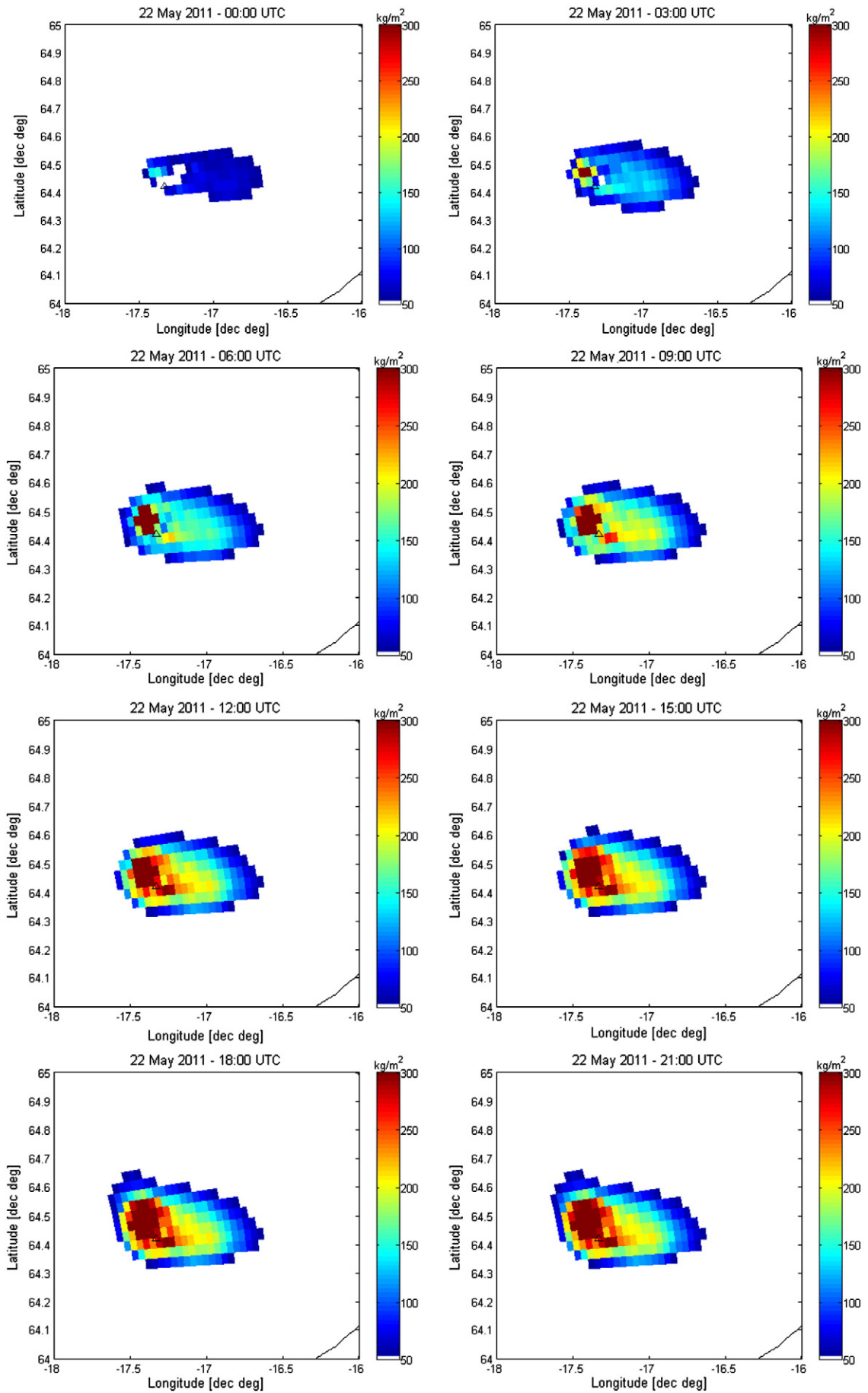


**Table 2**

Total mass and total volume values for the May 21–28, 2011 eruption period, obtained from radar-derived ashfall rate  $R_a$  by selecting fall velocity values  $a_v$  and  $b_v$ , derived from the Harris and Rose (1983) ash fallout (HAF) data and the Wilson (1972) ash fallout (WAF) data. Sensitivity of total mass volume to the standard deviation of estimated ashfall rate, indicated by  $\sigma(R_a)$ , is also shown.

Source	Fallout model	Total mass [kg]	Total volume [m <sup>3</sup> ]
VARR using $R_a - \sigma(R_a)$	HAF	$4.5968 \times 10^{11}$	$3.8307 \times 10^8$
VARR using $R_a$	HAF	$4.6535 \times 10^{11}$	$3.8779 \times 10^8$
VARR using $R_a + \sigma(R_a)$	HAF	$4.6549 \times 10^{11}$	$3.8791 \times 10^8$
VARR using $R_a - \sigma(R_a)$	WAF	$4.2487 \times 10^{11}$	$3.5406 \times 10^8$
VARR using $R_a$	WAF	$4.2384 \times 10^{11}$	$3.5320 \times 10^8$
VARR using $R_a + \sigma(R_a)$	WAF	$4.2511 \times 10^{11}$	$3.5426 \times 10^8$

considering: i) 2 different ash fallout models derived from Harris and Rose (1983) and from Wilson (1972); and ii) an uncertainty of the estimated ash fall rate  $R_a$  equal to minus or plus the estimation standard deviation, derived from estimation error analysis due to the best fit of the regression curve. Note that values in Table 2 of  $V_{at}$  are in the order of magnitude of  $3.5 \times 10^8$  m<sup>3</sup> and they well agree with the VEI-4 classification given to the 2011 Grímsvötn eruption. Indeed, values of eruption volume in the range [10<sup>8</sup>, 10<sup>9</sup>] m<sup>3</sup> are expected for a VEI-4 eruption.

For volcanological purposes, it would be of much interest to quantitatively compare the ground ash estimates between different eruptions, possibly using the same sensor and retrieval technique. To this aim, Fig. 9 shows the comparison between the total distal fallout spatial maps, retrieved by VARR, in terms of columnar ash content (kg m<sup>-2</sup>) between the Grímsvötn volcano eruption in 2011 (left panel, from May 21, 2011 at 23:55 UTC till May 28, 2011 at 23:55 UTC) and in 2004 (right panel, from 21:20 UTC on Nov. 1, 2004 till 09:55 UTC on Nov. 3, 2004). Note that the total distal fallout in 2011 has peaks up to ten times larger than in 2004 even though the latter had a duration which was five times longer.

#### 4. Satellite microwave radiometer signatures

Radar-derived retrievals cannot be compared with ground ash samples and drills due to unavailability of the latter till now. A comparison between radar-based estimates and corresponding ground ash sampling has been carried out for the previous 2004 Grímsvötn volcano eruption (Marzano et al., 2010a,b; Vogfjörð et al., 2005). As a matter of fact, most volcanoes are very often out of range of operational radar systems for meteorological monitoring. Satellite-based ultraviolet sensors are used to study volcanic gas clouds and infrared sensors are used to track and characterize volcanic ash clouds in the atmosphere for up to several days after an eruption. However, near the volcanic vent, most of volcanic ash clouds are opaque in the ultraviolet to infrared region and appear as thick as meteorological clouds. As a result, visible-infrared (VIS-IR) sensors aboard LEO and GEO satellites are of limited use in determining the particle size distribution and mass of these opaque volcanic ash clouds (Gangale et al., 2010; Wen & Rose, 1994).

In this respect, passive observations from microwave (MW) radiometers on LEO satellites can offer useful complementary information due to the relatively low microwave extinction and high thermal emission of ash clouds (Delene et al., 1996). This means that microwave brightness temperature (BT) is sensitive to the whole ash column and not only to the upper part as typical for VIS-IR radiometers both on LEO and GEO satellites. The major disadvantage of LEO microwave radiometers is the relatively poor spatial resolution

which is of the order of few kilometers around 180 GHz up to tens of kilometers around 30 GHz (Yan & Weng, 2008). It is worth mentioning that the remote sensing principle of MW radiometers is completely different from that of MW radars, the latter being an active sensor based on backscattering response whereas the first a passive sensor detecting the thermal emission and multiple scattering (e.g., Marzano et al., 1999; Wilheit et al., 1994).

In order to examine the sensitivity of MW BTs to the presence and intensity of ash clouds, the considered Icelandic sub-glacial Grímsvötn 2011 eruption case study is analyzed and discussed by using data from the Special Sensor Microwave Imager/Sounder (SSMIS). SSMIS is a conically scanning radiometers with a swath of about 1700 km aboard the LEO DMSP (United States Air Force Defense Meteorological Satellite Program) platform, firstly launched in 2003 (Yan & Weng, 2008). Currently 3 satellites ensure a repetition frequency over a given area of about three overpasses per day. Specifications of SSMIS are given in Table 3 in terms of frequency, polarization, along track and cross-track resolution, spatial sampling and instrumental noise.

Referring to horizontal and vertical polarization by H and V, respectively, Fig. 10 shows BT in (K) images at 37 V, 91 V, 150 H and  $183 \pm 6$  H GHz acquired by SSMIS aboard the F-16 DMSP satellite overpassing Iceland on May 21, 2011 at 08:46 UTC during the eruption of the Grímsvötn volcano. The BT depression, which is evident in all images around the volcano vent in terms of lower values with respect to the surrounding pixels, is the signature of the plume due to ash (and, if present, ice) particle scattering of the MW radiation emitted by the land/ocean background. The MW BT of this scene is clearly frequency and surface dependent: for example, the sea is relatively “cold” at 37 GHz due to the effect of quasi-specular surface low emissivity (Pulvirenti et al., 2007) and “warm” above 100 GHz due to the effect of atmospheric water vapor whose contribution is not anymore negligible at these frequencies (Wilheit et al., 1994). Note that the surface features can be misinterpreted: ice glaciers have a signature which can be ambiguous with respect to ash clouds, especially below 100 GHz due to the fact that both targets are relatively efficient scatters with a low emissivity (Grody & Basist, 1996). Surface BT effects are more evident below 100 GHz with a radiometric signature of the cloud-free ice cap (especially in north-west area with respect to the vent where the ash plume was not dispersed), whereas around 183 GHz the strong emission of water vapor tends to mask the surface itself, as evident in Fig. 10.

C-band radar data can be used as a ground reference for spaceborne MW BT imagery interpretation. Fig. 11 shows C-band radar PPI and RHI images at 08:30 and 08:35 UTC on May 22, 2011, close to the SSMIS images in Fig. 10. The radar reflectivity signature is limited around the volcano vent and this suggests the ambiguous contribution of frozen surface and ash cloud affecting the BT observations below 100 GHz. MW scattering indexes have been proposed in the past to identify scattering targets, especially rainfall (Delene et al., 1996; Spencer et al., 1989). The latter exhibits a behavior which is similar to ash clouds so that some of these scattering indexes can be tested for ash cloud identification as well.

Using the distinct features between the horizontally and vertically polarized BTs, it was noted that no-rain areas over the ocean can be identified under high polarization difference and rainy areas with little polarization difference. The PCT (Polarization-Corrected Temperature) parameter is then defined by (Spencer et al., 1989):

$$PCT = 1.818 \cdot BT_V(91) - 0.818 \cdot BT_H(91) \quad (8)$$

**Fig. 8.** Distal fallout spatial maps, retrieved by VARR, in terms of columnar ash content (kg m<sup>-2</sup>). The distributions show the accumulated ash mass at the ground every 3 h (from left to right, from top panel to bottom) from May 22, 2011 from 00:00 UTC till 21:00 UTC. The black edged triangle is centered in the exact position of the Grímsvötn volcano, whereas colorbars are chosen in order to match the different dynamic ranges of the distributions. (For interpretation of the references to color in this figure legend, the reader is referred to the web version of this article.)

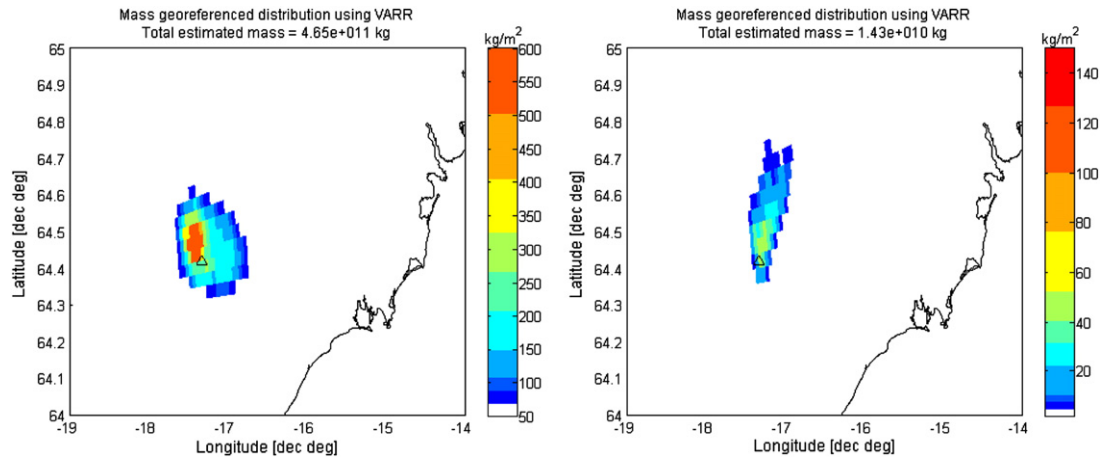


**Fig. 9.** Comparison between the total distal fallout spatial maps, retrieved by VARR, in terms of columnar ash content ( $\text{kg m}^{-2}$ ) between the Grímsvötn volcano eruption in 2011 (left panel, from May 21, 2011 at 23:55 UTC till May 28, 2011 at 23:55 UTC) and the Grímsvötn volcano eruption in 2004 (right panel, from 21:20 UTC on Nov. 1, 2004 till 09:55 UTC on Nov. 3, 2004).

where  $BT_P(f)$  is the SSMIS brightness temperature for the P-polarized channel with  $P=H$  or  $V$  at a frequency  $f$  equal to 91 GHz. Note that the original formula in Eq. (8) used the 85 GHz BT that was available on the precursor of SSMIS, i.e. the SSMI, and which we here assume to be similar to 91 GHz; different threshold values can be used to compensate for slight differences. The typical threshold for precipitation using 85 GHz BT is 255 K. The main advantage of the PCT method is its ability to reduce the effect of background surface emissivity, making it possible to delineate areas of rainfall over varying surface types.

The Scattering Index over Land (SIL) is computed by using the low-frequency channels (19 and 22 GHz) to estimate the 91 GHz BT for non-scattering conditions and then subtracting the observed 91 GHz BT. The more radiation the area scatters, the higher SIL is. The empirical formula for SIL is (Delene et al., 1996):

$$SIL = 451.88 - 0.44 \cdot BT_V(19) - 1.775 \cdot BT_V(22) + 0.00574 \cdot BT_V(22) - BT_V(91) \quad (9)$$

where, again, as in Eq. (8), we substituted 89 GHz with 91 GHz channel frequency.

Fig. 12 shows PCT and SIL at 91 GHz at 08:34 UTC on May 22, 2011 (both derived from imagery shown in Fig. 10). In this case threshold values for PCT and SIL have been set to 250 (maximum threshold) and 10 K (minimum threshold), respectively. In Fig. 12 it also superimposed the snow cover mask as retrieved from the same SSMI observations with an empirical threshold algorithm (Grody & Basist, 1996), fairly consistent with the monthly snow cover (in white) shown in panel e) of Fig. 1. The Grody–Basist snowcover detection algorithm is a decision tree based on the use of frequencies up to 90 GHz (it was developed before the launch of SSMIS) and empirically calibrated over a global scale. Since snowcover scatters high-frequency radiation, this signature provides the first step in the decision tree. Since scattering signatures also occur for precipitation, and for deserts and frozen ground surfaces when using vertical polarization, tests to filter out these conditions are applied. However, in addition to removing snow-free regions, some snow can be removed even though missing snowcover represents a small fraction of the total amount. Therefore, the snow covered surface identified by the Grody–Basist algorithm causes ambiguity in the detection of the ash cloud with PCT and SIL, as evident in Fig. 12.

**Table 3**  
Radiometric characteristics of the SSMIS (H: horizontal; V: vertical; RC: right circular).

Frequency (GHz)	Polarization (V, H, and RC)	Along-track resolution (km)	Cross-track resolution (km)	Spatial sampling (km×km)	Instrument noise (K)
19.35	H, V	73	47	45×74	0.35
22.235	V	73	47	45×74	0.45
37.0	H, V	41	31	28×45	0.22
50.3	H	17.6	27.3	37.5×37.5	0.34
52.8	H	17.6	27.3	37.5×37.5	0.32
53.596	H	17.6	27.3	37.5×37.5	0.33
54.4	H	17.6	27.3	37.5×37.5	0.33
55.5	H	17.6	27.3	37.5×37.5	0.34
57.29	RC	17.6	27.3	37.5×37.5	0.41
59.4	RC	17.6	27.3	37.5×37.5	0.40
63.283248 ± 0.285271	RC	17.6	27.3	75×75	2.7
60.792668 ± 0.357892	RC	17.6	27.3	75×75	2.7
60.792668 ± -0.357892 ± 0.002	RC	17.6	27.3	75×75	1.9
60.792668 ± 0.357892 ± 0.005	RC	17.6	27.3	75×75	1.3
60.792668 ± 0.357892 ± 0.016	RC	17.6	27.3	75×75	0.8
60.792668 ± 0.357892 ± 0.050	RC	17.6	27.3	75×75	0.9
91.665	H, V	14	13	13×16	0.19
150	H	14	13	13×16	0.53
183.311 ± 1	H	14	13	13×16	0.38
183.311 ± 3	H	14	13	13×16	0.39
183.311 ± 6.6	H	14	13	13×16	0.56

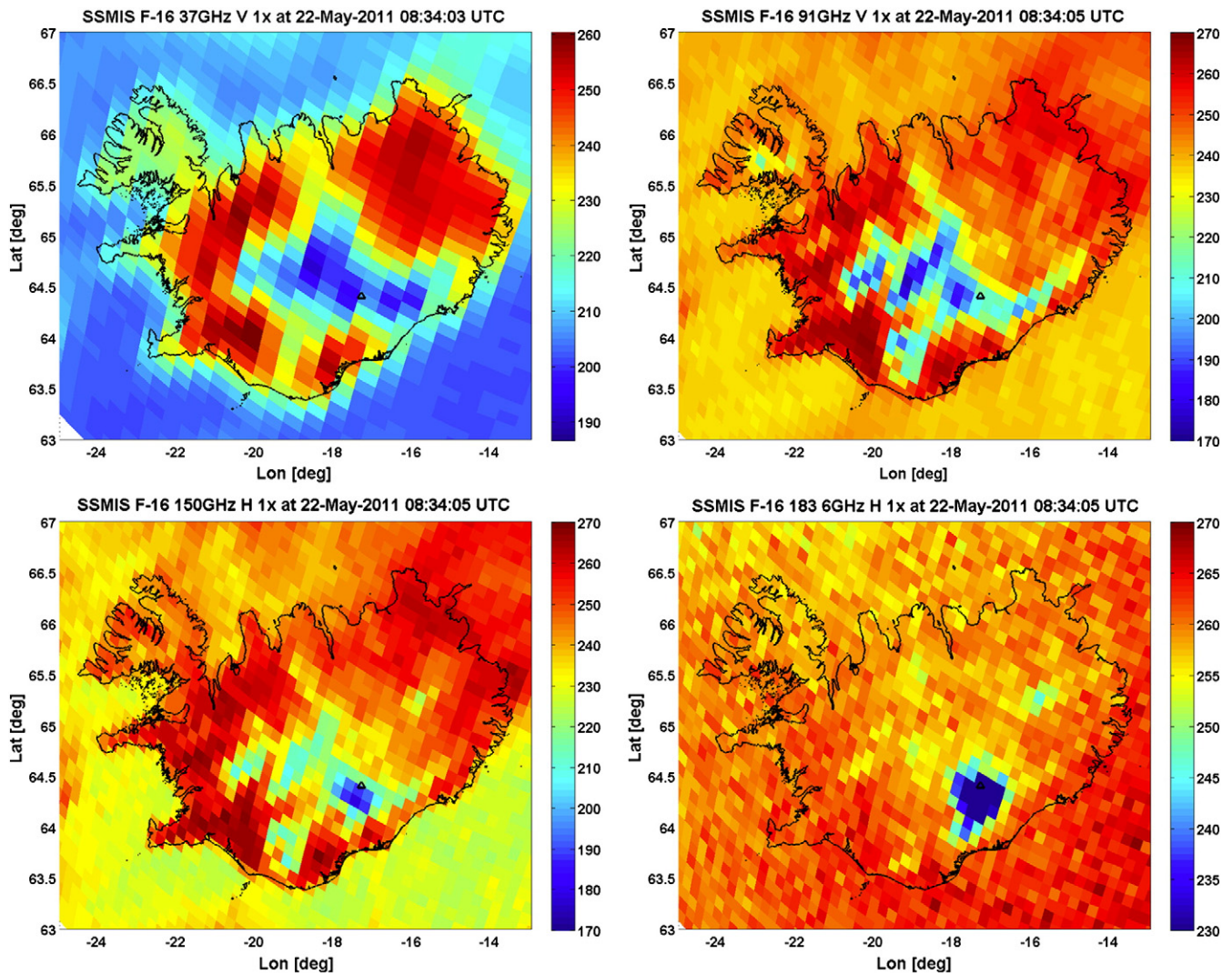


**Fig. 10.** Brightness temperature (BT, K) images at 37, 91, 150 and 183.6 GHz at vertical polarization, acquired by SSMIS (Special Microwave Imager Special) aboard the DMSP satellite on May 22, 2011 at 8:34 UTC during the eruption of the Grímsvötn volcano. The signature of the ash cloud is evident in all images around the volcano vent (indicated by a black triangle) as a depression of the measured BT with respect to the land BT due to tephra (and possible ice particles) scattering of land emitted radiation.

In order to detect ash plume within Icelandic scenario, it is most effective to exploit frequency indexes at frequencies higher than 90 GHz (which also show a relatively high and uniform spatial resolution for SSMIS: see Table 3) as the signatures at 150 and 183 GHz in Fig. 10 suggest. Two simple detection products can be derived from the SSMIS observations, hereafter named as the Absorption Microwave Spectral Difference ( $MSD_A$ ) and Window Microwave Spectral Difference ( $MSD_W$ ) and defined as follows:

$$\begin{cases} MSD_A = BT_H(183 \pm 6) - BT_H(183 \pm 1) \\ MSD_W = BT_H(150) - BT_H(91). \end{cases} \quad (10)$$

Fig. 13 shows these two indexes, obtained from the SSMIS observations at 08:46 UTC on May 21, 2011 in Fig. 10, assuming a minimum threshold of 0 K for both so that only positive values of  $MSD_A$  and  $MSD_W$  are considered. Note that the area where VARR detected non-zero ash concentration at 08:35 UTC (Fig. 11) is also indicated in Fig. 13. By comparing the ash detection results obtained in Fig. 13 with those of Fig. 12 it is apparent that MSDs (based on frequencies higher than 100 GHz) seem to better detect the ash plume dispersion with respect to both PCT and SIL, due to the effective mitigation of ambiguous snow surface signatures. The misplacement between the

radar-based signature in Fig. 11 and SSMIS detected area in Fig. 13 may depend not only on georeferencing errors (SSMIS image may be affected by an antenna mispointing of about 1 pixel which means about 20 km), but also by a different microphysical sensitivity. Indeed, BTs at frequencies above 90 GHz (wavelengths smaller than 3 mm) are mostly sensitive to fine ash particles of about 10–100  $\mu\text{m}$  which are suspended and dispersed in the middle and top layers of the troposphere, whereas C-band (wavelength of 6 cm) radar reflectivity  $Z_{Hm}$  basically responds to coarse ash and lapilli particles of about 0.1–10 mm which are falling in the surroundings of the volcanic area and are less subject to wind transportation. In addition, it is worth mentioning that the ash signature obtained by the MSD approach in Fig. 13 is quite consistent with the MODIS acquisition shown in Fig. 1 panels a and b. The latter, even though acquired nearly 3 h before the SSMI overpass, indicate the presence of ash in the south area with respect to the volcano vent.

The detection of ash cloud from space-based microwave BTs and the coregistration of SSMI and radar data can provide a first attempt to quantitatively link microwave BTs with measured copolar radar reflectivity  $Z_{Hm}$ . Note that for a direct comparison of ground-based radar and satellite radiometer observations, it is necessary to spatially average and downsample the measured reflectivity to the SSMIS

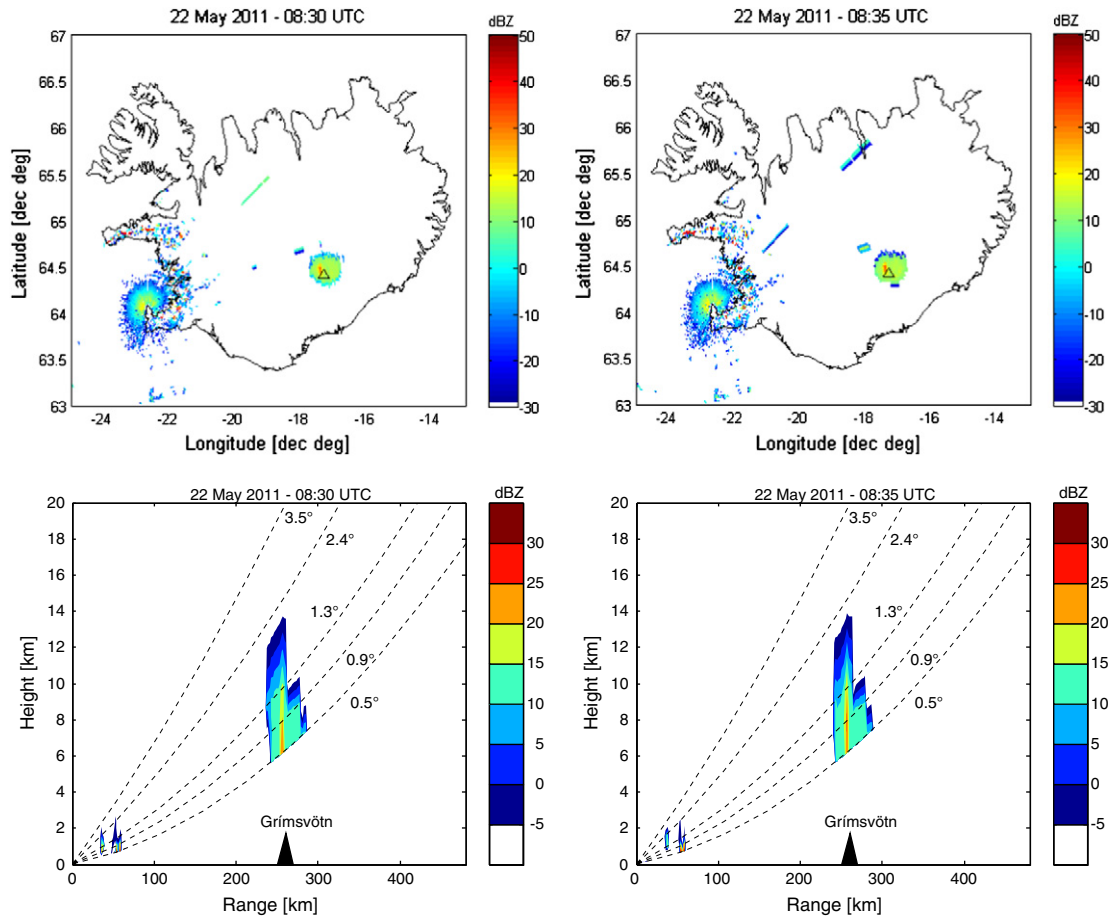


**Fig. 11.** Radar PPI images (top panels) and corresponding RHI images along the radar-vent line (bottom panels) at 08:30 UTC (left panels) and 8:35 UTC (right panels) on May 22, 2011.

footprint which is about  $13 \times 14 \text{ km}^2$  (see Table 3). This means that the PPI image in Fig. 11 has been further filtered to a resolution of  $14 \times 14 \text{ km}^2$  from the available resolution at  $2 \times 2 \text{ km}^2$ .

The instantaneous  $C_a$  values, obtained by means of the VARR technique, have been vertically integrated to estimate the ash columnar content (ACC). Fig. 14 shows the empirical correlation diagram of

ACC versus both window and absorbed SSMIS BT channels (above 90 GHz), extracted from the matching of data in Fig. 13. The correlation coefficient of BTs at  $91, 150, 183 \pm 6$  and  $183 \pm 1$  GHz with ACC is, respectively,  $-0.37, -0.52, -0.48$  and  $-0.63$ . It is worth noting the relatively high correlation between ACC and absorbed channels around 183 GHz due to high clear-air opacity and surface insensitivity.

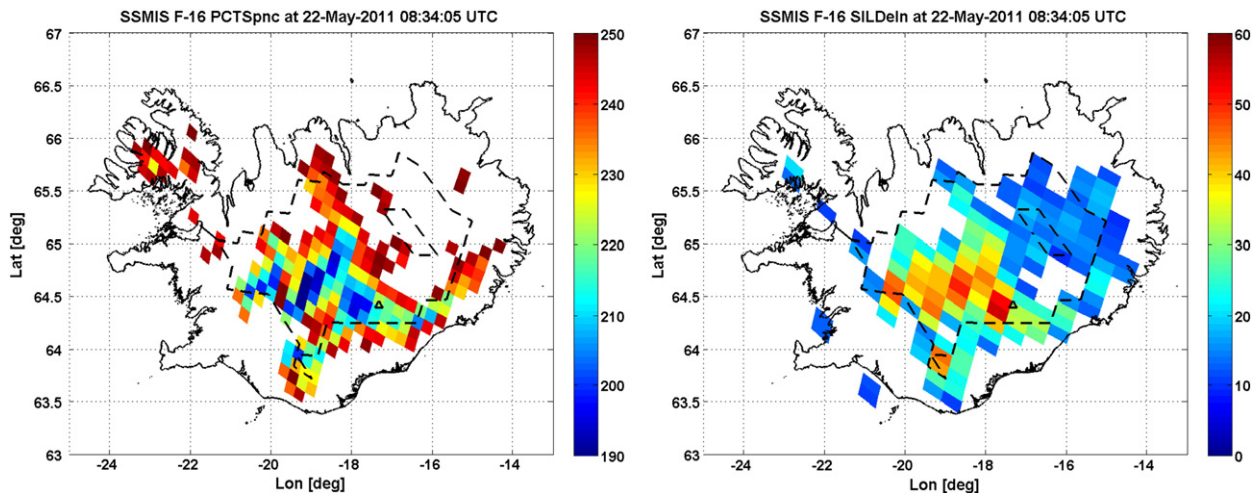


**Fig. 12.** (Left panel) Polarized-Corrected Temperature (PCT) at 91 GHz at 08:34 UTC on May 21, 2011, derived from imagery shown in Fig. 10. (Right panel) Scattering Index over Land (SIL) at 91 GHz at 08:34 UTC on May 21, 2011, derived from imagery shown in Fig. 10. Dashed lines indicate the snow cover mask as retrieved from SSMIS imagery with the algorithm described in Grody and Basist (1996).

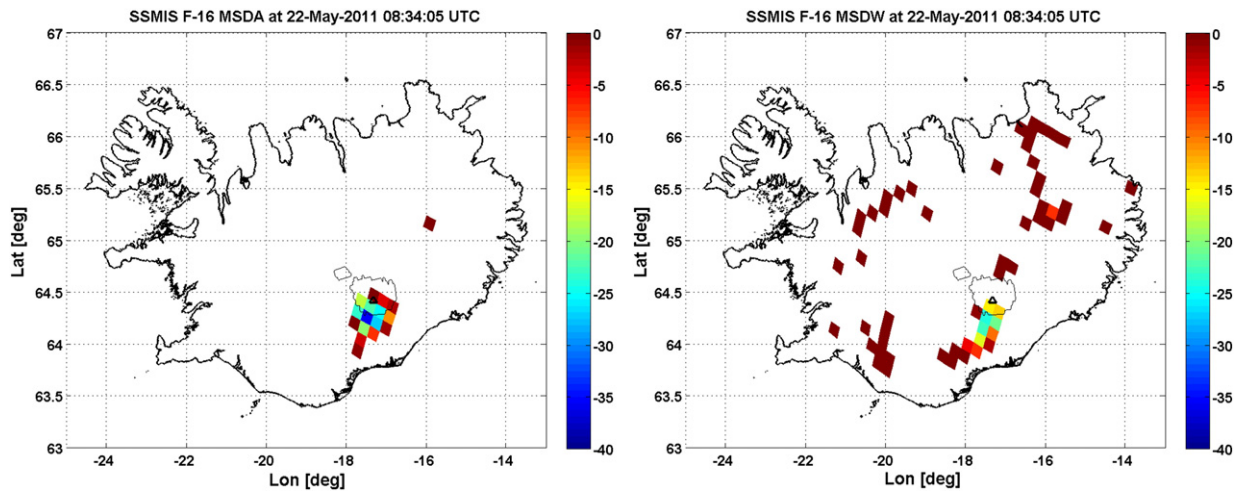


Fig. 13. Microwave Spectral Difference at absorption bands (left panel:  $MSD_A = TB_{183} \pm 6 - TB_{183} \pm 1$ ) and at Window bands (right panel:  $MSD_W = TB_{150H} - TB_{91H}$ ) at 08:34 UTC on May 21, 2011, derived from imagery shown in Fig. 10 (see text for details). The solid thin line indicates the area where VARR detected non-zero ash concentration around 08:35 UTC.

By exploiting the latter result, Fig. 15 shows the ACC, computed from  $C_a$  profiles estimated by VARR around 08:35 UTC, i.e. the SSMI overpass on May 22, 2011, compared with that one estimated from SSMIS observations at  $183 \pm 1$  GHz using a regressive estimator based on the  $BT_H(183 \pm 1$  GHz) and its linear correlation with ACC (as obtained in Fig. 14):

$$I_a = a + bBT_H(183 \pm 1) \quad (11)$$

where  $I_a$  is the vertically-integrated (columnar) ash content and  $a$ ,  $b$  are the regression coefficients which are independent of the surface background, but influenced by the columnar water vapor of the scene. Results of Fig. 15 may be physically questionable if we refer to the different microphysical sensitivity between BTs and Zs, as discussed before. It should be noted, however, that the radar sensitivity is significantly increased by performing a spatial average to SSMIS footprint so that the ash signature detected by the two instruments tends to be more physically consistent.

## 5. Conclusions

The sub-glacial Plinian explosive eruption of the Grímsvötn volcano on May 2011 has been analyzed and quantitatively interpreted by using ground-based weather radar data and the Volcanic Ash Radar

Retrieval (VARR) technique. Physical principles, inversion methodology and practical limitations and potentials of the VARR approach for single-polarization Doppler radars have been pointed out and discussed. The 2011 Grímsvötn eruption has been continuously monitored by the Keflavík C-band weather radar, located at a distance of about 260 km from the volcano vent. The VARR methodology has been applied to Keflavík C-band available radar time series to estimate the plume maximum height, ash particle category, ash volume, ash fallout and ash concentration every 5 min near the vent. Estimates of the eruption discharge rate, based on the retrieved ash plume top height, have been provided together with an evaluation of the total erupted mass and volume. Deposited ash loading has been also retrieved from radar data by empirically reconstructing the vertical profile of radar reflectivity and estimating the near-surface ash fallout. Radar-based retrieval results have not been compared with ground measurements, due to the lack of the latter, but they have been qualitatively compared with available microwave radiometric imagery in order to preliminarily show the unique contribution of these microwave remote sensing products to the understating and modeling of explosive volcanic ash eruptions.

Future developments should be devoted to the exploitation of dual-polarized weather radars, capable of measuring polarimetric observables both in amplitude and phase, for increasing the ash retrieval sensitivity and accuracy nearby the volcanic vent. Mixtures of

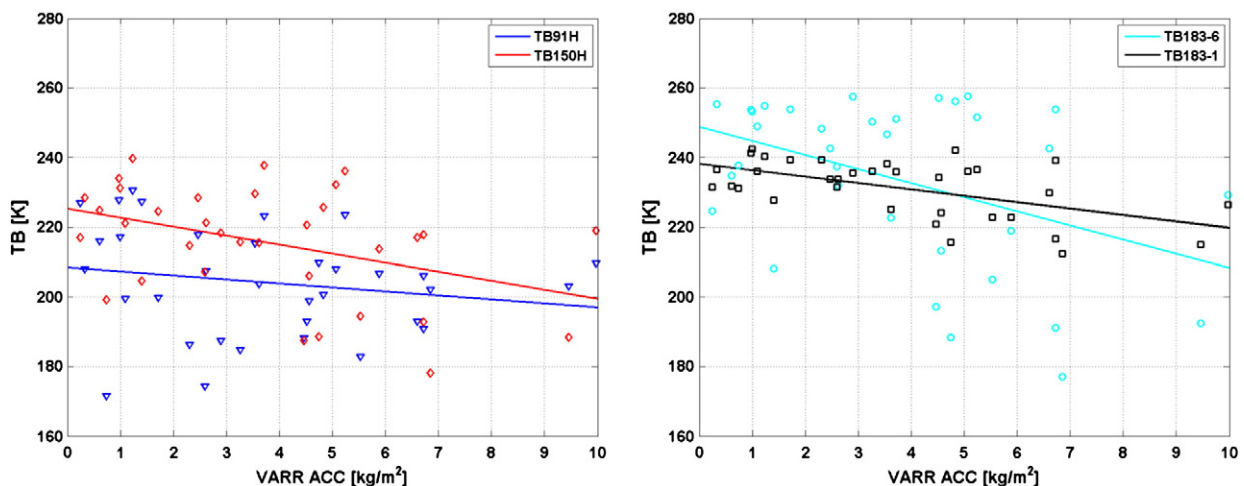
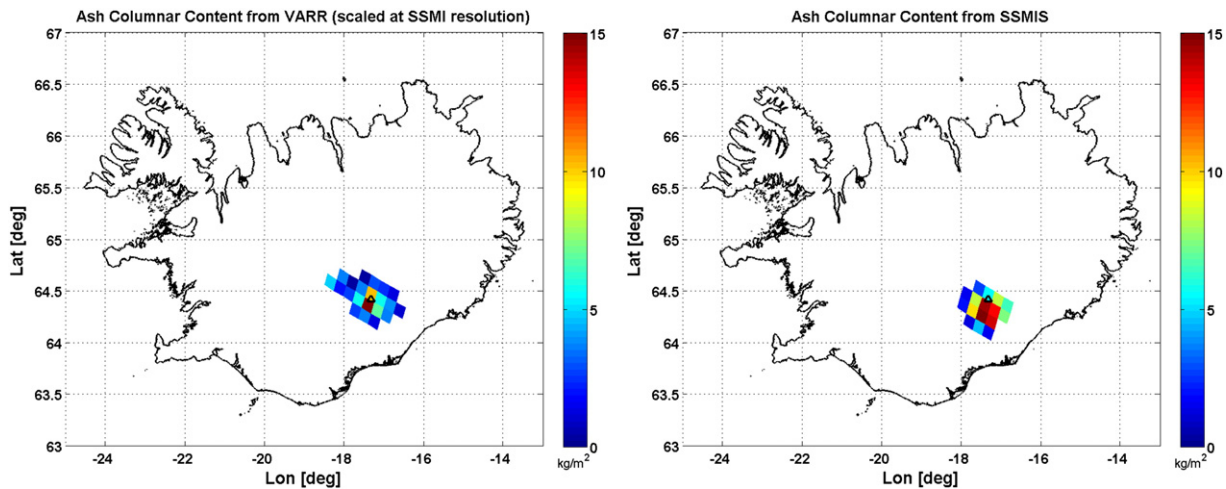


Fig. 14. Empirical correlation diagram of ash columnar content versus BT at window (left) and absorption (right) channels.



**Fig. 15.** (Left panel) Ash columnar content, computed from  $C_a$  profiles estimated by VARR around 08:35 UTC on May 21, 2011 and scaled onto the resolution of SSMIS. (Right panel) Estimated ash columnar content from SSMIS  $183 \pm 1$  GHz observations at 08:34 UTC using the linear correlation found in Fig. 14.

hydrometeors and ash, undistinguishable from pure ash clouds using conventional radars, could be better investigated using dual-polarization instruments at higher frequencies. In this respect, weather radars at X-band might even show a better sensitivity with respect to the corresponding C-band systems having the same characteristics. The synergy among ground-based and satellite-based sensors should be further investigated as measurements from visible/infrared satellite imagers and ground-based lidars may be used as a complementary constraint for radar-based estimates due to their high sensitivity to fine ash particles.

### Acknowledgments

We are grateful to B. Palmason and S. Karlsdóttir (Iceland Meteorological Office, Reykjavik, Iceland) for providing radar data and Rainbow® software products. The contributions of B. De Bernardinis (ISPRA, Rome, Italy), G. Vulpiani (DPC, Rome, Italy), E. Picciotti (HIMET, L'Aquila, Italy) and S. Di Fabio (CETEMPS; L'Aquila, Italy) are gratefully acknowledged. This work has been partially funded by the Italian Department of Civil Protection (DPC), Rome, Italy within the IDRA2 project, by the Sapienza University of Rome, Italy, and by the Marie Curie Fellowship within the call FP7-PEOPLE-2010-IEF, grant number: 273666.

### References

Bonadonna, C., & Houghton, B. F. (2005). Total grain-size distribution and volume of tephra-fall deposits. *Bulletin of Volcanology*, 67(10), 441–456.

Delene, D. J., Rose, W. I., & Grody, N. C. (1996). Remote sensing of volcanic clouds using special sensor microwave imager data. *Journal of Geophysical Research*, 101(B5), 11579–11588.

Gangale, G., Prata, A. J., & Clarisse, L. (2010). The infrared spectral signature of volcanic ash determined from high-spectral resolution satellite measurements. *Remote Sensing of Environment*, 114(2), 414–425.

Gouhier, M., & Donnadieu, F. (2008). Mass estimations of ejecta from Strombolian explosions by inversion of Doppler radar measurements. *Journal of Geophysical Research*, 113(B10202), 10202–10219.

Grody, N. C., & Basist, A. N. (1996). Global identification of snowcover using SSM/I measurements. *IEEE Transactions on Geoscience and Remote Sensing*, 34(1), 237–249.

Harris, D. M., & Rose, W. I., Jr. (1983). Estimating particle sizes, concentrations, and total mass of ash in volcanic clouds using weather radar. *Journal of Geophysical Research*, 88(C15), 10969–10983.

Hort, M., Seyfried, R., & Vöge, M. (2003). Radar Doppler velocimetry of volcanic eruptions: Theoretical considerations and quantitative documentation of changes in eruptive behaviour at Stromboli volcano, Italy. *Geophysical Journal International*, 154(2), 515–532.

Kitchen, M., & Jackson, P. M. (1993). Weather radar performance at long range. Simulated and observed. *Journal of Applied Meteorology*, 32, 975–985.

Lacasse, C., Karlsdóttir, S., Larsen, G., Soosalu, H., Rose, W. I., & Ernst, G. G. J. (2004). Weather radar observations of the Hekla 2000 eruption cloud, Iceland. *Bulletin of Volcanology*, 66(10), 457–473.

Larsen, G., Guðmundsson, M. T., & Björnsson, H. (1998). Eight centuries of periodic volcanism at the center of the Iceland hotspot revealed by glacier tephrostratigraphy. *Geology*, 26(10), 943–946.

Marzano, F. S., Barbieri, S., Picciotti, E., & Karlsdóttir, S. (2010a). Monitoring sub-glacial volcanic eruption using C-band radar imagery. *IEEE Transactions on Geoscience and Remote Sensing*, 58(1), 403–414.

Marzano, F. S., Barbieri, S., Vulpiani, G., & Rose, W. I. (2006b). Volcanic ash cloud retrieval by ground-based microwave weather radar. *IEEE Transactions on Geoscience and Remote Sensing*, 44(11), 3235–3246.

Marzano, F. S., Lamantea, M., Montopoli, M., Di Fabio, S., & Picciotti, E. (2011). The Eyjafjöll explosive volcanic eruption from a microwave weather radar perspective. *Atmospheric Chemistry and Physics*, 11(18), 9503–9518.

Marzano, F. S., Lamantea, M., Montopoli, M., Oddsson, B., & Gudmundsson, M. T. (2012b). Validating sub-glacial volcanic eruption using ground-based C-band radar imagery. *IEEE Transactions on Geoscience and Remote Sensing*, 50. <http://dx.doi.org/10.1109/TGRS.2011.2167017>.

Marzano, F. S., Marchiotti, S., Textor, C., & Schneider, D. (2010b). Model-based weather RADAR remote sensing of explosive volcanic ash eruption. *IEEE Transactions on Geoscience and Remote Sensing*, 48(10), 3591–3607.

Marzano, F. S., Mugnai, A., Panegrossi, G., Pierdicca, N., Smith, E. A., & Turk, J. (1999). Bayesian estimation of precipitating cloud parameters from combined measurements of spaceborne microwave radiometer and radar. *IEEE Transactions on Geoscience and Remote Sensing*, 37(1), 596–613.

Marzano, F. S., Picciotti, E., Vulpiani, G., & Montopoli, M. (2012a). Synthetic signatures of volcanic ash cloud particles from X-band dual-polarization radar. *IEEE Transactions on Geoscience and Remote Sensing*, 50(1), 193–211.

Marzano, F. S., Vulpiani, G., & Rose, W. I. (2006a). Microphysical characterization of microwave radar reflectivity due to volcanic ash clouds. *IEEE Transactions on Geoscience and Remote Sensing*, 44(2), 313–327.

Morton, R. R., Taylor, G., F.R.S., & Turner, J. S. (1956). Turbulent gravitational convection from maintained and instantaneous sources. *Proceedings of the Royal Society of London. Series A: Mathematical and Physical Sciences*, 234(1196), 1–23.

Oddsson, B., Guðmundsson, M. T., Larsen, G., & Karlsdóttir, S. (2008). Grímsvötn 2004: Weather radar records and plume transport models applied to a phreatomagmatic basaltic eruption. *IAVCEI 2008, Reykjavik (Iceland)*, August 18–24, 2008.

Oddsson, B., Gudmundsson, M., Larsen, G., & Karlsdóttir, S. (2012). Monitoring of the plume from the basaltic phreatomagmatic 2004 Grímsvötn eruption — Application of weather radar and comparison with plume models. *Bulletin of Volcanology*, 74(6), 1395–1407.

Prata, A. J., Barton, I. J., Johnson, R. W., Kamo, K., & Kingwell, J. (1991). Hazard from volcanic ash. *Nature*, 354(25).

Pulvirenti, L., Marzano, F. S., & Pierdicca, N. (2007). Modeling microwave fully-polarimetric passive observations of a sea surface: A neural network approach. *IEEE Transactions on Geoscience and Remote Sensing*, 45(7), 2098–2117 (ISSN: 0196-2892).

Rodgers, C. D. (2000). *Inverse methods for atmospheric sounding. Theory and practice*. Singapore: World Scientific Publishing.

Rose, W. I., Kostinski, A. B., & Kelley, L. (1995). Real time C band radar observations of 1992 eruption clouds from Crater Peak, Mount Spurr Volcano, Alaska. *U.S. Geological Survey Bulletin*, 2139, 19–26.

Sauvageot, H. (1992). *Radar meteorology*. Boston: Artech House Radar Library.

Showstack, R. (2011). Iceland's Grímsvötn volcano erupts. *EOS, Transactions American Geophysical Union*, 92(22), 187.

Sparks, R. (1986). The dimensions and dynamics of volcanic eruption columns. *Bulletin of Volcanology*, 48(1), 3–15.

Sparks, R. S. J., Bursik, M. I., Carey, S. N., Gilbert, J. S., Glaze, L., Sigurðsson, H., et al. (1997). *Volcanic plumes*. New York: John Wiley and Sons Ltd.

Spencer, R. W., Goodman, H. M., & Hood, R. E. (1989). Precipitation retrieval over land and ocean with the SSM/I — Identification and characteristics of the scattering signal. *Journal of Atmospheric and Oceanic Technology*, 6(2), 254–273.

- Stewart, S. F., Pinkerton, H., Blackburn, G. A., & Guðmundsson, M. T. (2008). Monitoring active subglacial volcanoes: A case study using airborne remotely sensed imagery of Grímsvötn, Iceland. *International Journal of Remote Sensing*, 29(22), 6501–6514.
- Stohl, A., Prata, A. J., Eckhardt, S., Clarisse, L., Durant, A., Henne, S., et al. (2011). Determination of time- and height-resolved volcanic ash emissions and their use for quantitative ash dispersion modeling: The 2010 Eyjafjallajökull eruption. *Atmospheric Chemistry and Physics*, 11(9), 5541–5588.
- Thordarson, T., & Larsen, G. (2007). Volcanism in Iceland in historical time: Volcano types, eruption styles and eruptive history. *Journal of Geodynamics*, 43(1), 118–152.
- Tupper, A., Itikarai, I., Richards, M., Prata, F., Carn, S., & Rosenfeld, D. (2007). Facing the challenges of the international airways volcano watch: The 2004/05 eruptions of Manam, Papua New Guinea. *Weather and Forecasting*, 22(1), 175–191.
- Vogfjörð, K., Jakobsdóttir, S., Guðmundsson, G. B., Roberts, M. J., Ágústsson, K., Arason, T., et al. (2005). Forecasting and monitoring a subglacial eruption in Iceland. *EOS, Transactions American Geophysical Union*, 86(26), 245–252.
- Vulpiani, G., Montopoli, M., Picciotti, E., & Marzano, F. S. (2011). On the use of a polarimetric X-band weather radar for volcanic ash clouds monitoring. *AMS Radar Conference, Pittsburgh (PA – USA), September 26–30, 2011*.
- Wen, S., & Rose, W. I. (1994). Retrieval of sizes and total masses of particles in volcanic clouds using AVHRR bands 4 and 5. *Journal of Geophysical Research*, 99(D3), 5421–5431.
- Wilheit, T., Adler, R., Avery, S., Barrett, E., Bauer, P., Berg, W., et al. (1994). Algorithms for the retrieval of rainfall from passive microwave measurements. *Remote Sensing Reviews*, 11(1–4), 163–194.
- Wilson, L. (1972). Explosive volcanic eruptions—II: The atmospheric trajectories of pyroclasts. *Geophysical Journal of the Royal Astronomical Society*, 30(2), 381–392.
- Wilson, L., Sparks, R. S. J., Huang, T. C., & Watkins, N. D. (1978). The control of volcanic column heights by eruption energetics and dynamics. *Journal of Geophysical Research*, 83(B4), 1829–1836.
- Yan, B., & Weng, F. (2008). Intercalibration between special sensor microwave imager/sounder and special sensor microwave imager. *IEEE Transactions on Geoscience and Remote Sensing*, 46(9), 984–995.
- Yu, T., Rose, W. I., & Prata, A. J. (2002). Atmospheric correction for satellite based volcanic ash mapping and retrievals using “split-window” IR data from GOES and AVHRR. *Journal of Geophysical Research*, 107(D16), 4311–4330.
- Zehner, C. (Ed.). (2010). *Monitoring volcanic ash from space. Proceedings of the ESA-EUMETSAT workshop on the 14 April to 23 May 2010 eruption at the Eyjafjöll volcano, South Iceland. Frascati, Italy, 26–27 May 2010. <http://dx.doi.org/10.5270/atmch-10-01>* (ESA-Publication STM-280).
- Zrnic, D. S., & Ryzkov, A. (1996). Advantages of rain measurements using specific differential phase. *Journal of Atmospheric and Oceanic Technology*, 13, 454–464.